

EVIDENCES OF THE PHOTOSPHERE EMISSION ORIGIN FOR THE GAMMA-RAY BURST PROMPT EMISSION

YAN-ZHI MENG^{1,2}

¹School of Astronomy and Space Science, Nanjing University, Nanjing 210023, China; yzmeng@nju.edu.cn and

²Key Laboratory of Modern Astronomy and Astrophysics (Nanjing University), Ministry of Education, China

Draft version April 5, 2022

ABSTRACT

The physical origin of gamma-ray burst (GRB) prompt emission is still subject to debate after five decades (photosphere or synchrotron). Here, firstly we find that many observed characteristics of 15 long GRBs, which have the highest prompt emission efficiency ϵ_γ ($\epsilon_\gamma \gtrsim 80\%$), strongly support the photosphere (thermal) emission origin: (1) The relation between E_p and E_{iso} is almost $E_p \propto (E_{iso})^{1/4}$, and the dispersion is quite small. (2) The simple power-law shape of the X-ray afterglow light curves and the significant reverse shock signals in the optical afterglow light curves. (3) Best-fitted by the cutoff power-law model for the time-integrated spectrum. (4) The consistent efficiency from observation (with E_{iso}/E_k) and the prediction of photosphere emission model (with η/Γ). Then, we further investigate the characteristics of the long GRBs for two distinguished samples ($\epsilon_\gamma \gtrsim 50\%$ and $\epsilon_\gamma \lesssim 50\%$). It is found that the different distributions for E_p and E_{iso} , and the similar observed efficiency (from the X-ray afterglow) and theoretically predicted efficiency (from the prompt emission or the optical afterglow) well follow the prediction of photosphere emission model. Also, based on the same efficiency, we derive an excellent correlation of $\Gamma \propto E_{iso}^{1/8} E_p^{1/2} / (T_{90})^{1/4}$ to estimate Γ . Finally, the different distributions for E_p and E_{iso} , and the consistent efficiency exist for the short GRBs. Besides, we give a natural explanation of the extended emission ($\epsilon_\gamma \lesssim 50\%$) and the main pulse ($\epsilon_\gamma \gtrsim 50\%$).

Subject headings: gamma-ray burst: general – radiation mechanisms: thermal – radiative transfer – scattering

1. INTRODUCTION

After more than 50 years since the discovery, the radiation mechanism of GRB prompt emission (photosphere emission or synchrotron emission) is still un-identified (e.g., Zhang & Yan 2011; Uhm & Zhang 2014; Geng et al. 2018, 2019; Lin et al. 2018; Zhang et al. 2018a,b, 2021; Li et al. 2019b, 2021; Burgess et al. 2020; Yang et al. 2020; Zhang 2020; Vyas et al. 2021; Zhang et al. 2021b). The photospheric emission is the basic prediction of the classical fireball model (Goodman 1986; Paczynski 1986) for GRB, because the optical depth τ at the jet base is much larger than unity (e.g. Piran 1999). As the fireball expands and the optical depth drops down, the internally trapped thermal photons finally escape at the photosphere ($\tau = 1$). Indeed, based on the spectral analysis, a quasi-thermal component has been found in several *Swift* GRBs (Ryde 2004, 2005; Ryde & Pe'er 2009) and *Fermi* GRBs (Guiriec et al. 2011, 2013; Axelsson et al. 2012; Ghirlanda et al. 2013; Larsson et al. 2015), especially in GRB 090902B (Abdo et al. 2009; Ryde et al. 2010; Zhang 2011). But whether the typical observed Band function (smoothly joint broken power law) (Band et al. 1993) or cutoff power law can be explained by the photosphere emission, namely the photospheric emission model, remains unknown (e.g., Abramowicz et al. 1991; Thompson 1994; Mészáros & Rees 2000; Rees & Mészáros 2005; Pe'er & Ryde 2011; Fan et al. 2012; Lazzati et al. 2013; Ruffini et al. 2013; Gao et al. 2015; Bégué & Pe'er 2015; Pe'er et al. 2015; Ryde et al. 2017; Acuner & Ryde 2018; Hou et al. 2018; Meng et al. 2018, 2019, 2022; Li 2019a,c, 2020; Acuner et al. 2020; Dereli-Bégué et al. 2020; Vereshchagin & Siutsou 2020; Wang et al.

2020; Parsotan & Lazzati 2022; Song & Meng 2022). If this scenario is true, the quasi-thermal spectrum should be broadened. Theoretically, two different broadening mechanisms have been proposed (see Appendix A): sub-photospheric dissipation (namely the dissipative photosphere model (Rees & Mészáros 2005; Giannios & Spruit 2007; Vurm & Beloborodov 2016; Beloborodov 2017), or geometric broadening (namely the probability photosphere model, Pe'er 2008; Pe'er & Ryde 2011; Lundman et al. 2013; Deng & Zhang 2014; Meng et al. 2018, 2019, 2022).

Previously, some implications from the statistical properties of the spectral analysis results for large GRB sample seem to support the photosphere emission model. First, lots of bursts have a low-energy spectral index α harder than the death line (or the maximum value, $\alpha = -2/3$) of the basic synchrotron model, especially for the short GRBs and the peak-flux spectrum (Kaneko et al. 2006; Zhang et al. 2011; Burgess et al. 2017). Second, the spectral width is found to be quite narrow for a significant fraction of GRBs (Axelsson & Borgonovo 2015; Yu et al. 2015). Third, for a half or more of GRBs, the cutoff power law is the best-fit empirical model (Goldstein et al. 2012; Gruber et al. 2014; Yu et al. 2016), indicating that the photosphere emission model can naturally interpret their high-energy spectrum. Here, we find more convincing evidences for the photosphere emission (especially the probability photosphere model) origin of the GRB prompt emission in this work.

The paper is organized as follows. In Section 2, we describe the evidences in the long GRBs with extremely high prompt efficiency ϵ_γ ($\epsilon_\gamma \gtrsim 80\%$). Then, in Section

3, the evidences in the long GRBs with $\epsilon_\gamma \gtrsim 50\%$ and $\epsilon_\gamma \lesssim 50\%$ are shown. In Section 4, we illustrate the evidences in the short GRBs. A brief summary is provided in Section 5.

2. EVIDENCES IN THE LONG GRBS WITH EXTREMELY HIGH EFFICIENCY ($\epsilon_\gamma \gtrsim 80\%$)

There is a lot of controversy for the spectral difference between the photosphere emission model and the synchrotron emission model, after considering the more natural and complicated physical conditions (jet structure, decaying magnetic field, and so on (e.g., Uhm & Zhang 2014; Geng et al. 2018; Meng et al. 2018, 2019, 2022). But a crucial difference between these two models is that the photosphere emission model predicts much higher radiation efficiency of prompt emission ϵ_γ , generally defined as $E_\gamma/(E_\gamma + E_k)$. Here, E_γ is the radiated energy in the prompt phase and E_k is the remaining kinetic energy in the afterglow phase. The synchrotron emission models mainly include the internal shock model (for a matter-dominated fireball, Rees & Meszaros 1994) and the ICMART model (internal-collision-induced magnetic reconnection and turbulence, for a Poynting-flux-dominated outflow, Zhang & Yan 2011). For the internal shock model, since only the relative kinetic energy between different shells can be released, the radiation efficiency is rather low ($\sim 10\%$, Kobayashi et al. 1997). For the ICMART model, the radiation efficiency can be much higher ($\sim 50\%$), and reaches $\sim 80\%$ in extreme case. But the extremely high ϵ_γ ($\epsilon_\gamma \gtrsim 80\%$) is unlikely to be achieved because the magnetic reconnection needs some conditions to trigger so that there is surely a lot of magnetic energy to be left. For the photosphere emission model, if only the acceleration is in the unsaturated regime ($R_{\text{ph}} < R_s$), the radiation efficiency can be close to 100%. Here, R_{ph} is the photospheric radius and R_s is the saturation acceleration radius. Thus, in this work, we select the GRBs with extremely high ϵ_γ ($\epsilon_\gamma \gtrsim 80\%$) (see Figure 1(a) and Table 1), since theoretically their prompt emission is likely to be produced by the photosphere emission. Considering that, $L_{X,11h}$ is roughly proportional to the E_k (see Appendix B1). To perform the selection, we calculated the $L_{X,11h}$, the late-time X-ray afterglow luminosity at 11 hours, for the large GRB sample (117 bursts, after GRB 110213A) with redshift¹. The calculated method (see Appendix B1) follows that in D'Avanzo et al. (2012), where the $L_{X,11h}$ for the other large GRB sample (46 bursts, before GRB 110213A, 5 other high-efficiency bursts selected) is given. Also, the 2 bursts (GRB 990705 and GRB 000210), claimed to have extremely high ϵ_γ in Lloyd-Ronning & Zhang (2004) is included. The E_{iso} is mainly taken from Minaev & Pozanenko (2020); Xue et al. (2019). We then analyze the prompt² and afterglow³ properties of these 15 long GRBs to confirm the photosphere emission origin.

¹ The redshift data are publicly available at <http://www.mpe.mpg.de/jcg/grbgen.html>.

² The *Fermi*/GBM data are publicly available at <https://heasarc.gsfc.nasa.gov/W3Browse/fermi/fermigbrst.html>. The Konus-Wind data are publicly available at <https://vizier.cds.unistra.fr/viz-bin/VizieR?-source=J/ApJ/850/161>.

³ The X-ray afterglow data are publicly available at https://www.swift.ac.uk/xrt_products/. The optical afterglow data are taken from Li et al. (2012, 2018); Liang et al. (2013).

2.1. Characteristics of Prompt Emission

For the photosphere emission model, the peak energy of the observed spectrum E_p corresponds to the temperature of the observed blackbody T_{ob} . In the unsaturated regime ($R_{\text{ph}} < R_s$), the observed temperature $T_{\text{ob}} = D \cdot T_{\text{comoving}} = \Gamma \cdot (T_0/\Gamma) = T_0$. Here, D is the Doppler factor, T_{comoving} is the photon temperature in the outflow comoving frame, Γ is the Lorentz factor of the outflow and T_0 is the temperature at the outflow base. Since $T_0 \propto (E_{\text{iso}})^{1/4}$, we should have $E_p \propto (E_{\text{iso}})^{1/4}$, here E_{iso} is the isotropic energy. Note that, $E_p = (1+z) \cdot E_{\text{ob}}$, after considering the redshift effect. In Figure 1(b), we plot the E_p and E_{iso} distributions of the selected GRBs (omitting GRB 081203A and GRB 130606A, because of the large E_p error), and find that they follow the predicted $E_p \propto (E_{\text{iso}})^{1/4}$ relation quite well. The best-fit result is $\log (E_p) = 2.54 + 0.25 \log (E_{\text{iso}})$. In Figure 1(c), we compare the E_p and E_{iso} distributions of the selected GRBs with those of the large sample of long GRBs, and find that the dispersion is quite small relative to that of the large sample.

In Figure 1(d), we plot the E_p and L_{iso} (the isotropic luminosity) distributions of the selected GRBs, and find that they follow the $E_p \propto (L_{\text{iso}})^{1/4}$ relation well, also. The best-fit result is $\log (E_p) = 2.75 + 0.23 \log (L_{\text{iso}})$. And the dispersion is found to be similar to that of $E_p \propto (E_{\text{iso}})^{1/4}$. Furthermore, based on the best-fit $E_p \sim 10^{2.75} \cdot (L_{\text{iso}})^{1/4}$ and $E_p = 2.7kT_0 = 2.7k(L_{\text{iso}}/4\pi r_0^2 ac)^{1/4}$, we obtain the initial acceleration radius $r_0 \sim 3.21 \times 10^8$ cm, well consistent with the quite high mean value $\langle r_0 \rangle \sim 10^{8.5}$ cm deduced in Pe'er et al. (2015).

In Figure 5, we show the E_p evolutions of the time-resolved spectra for 5 GRBs detected by Fermi/GBM. The E_p evolutions are found to follow the evolution of the flux F quite well (intensity tracking pattern, Liang & Kargatis 1996). This is consistent with the above-mentioned unsaturated acceleration condition of the photosphere emission. From Table 1 and 2, we can see that the best-fit spectral models of the time-integrated spectrum are the cutoff power law (COM) model or the high-energy spectral index β (using the BAND function to fit) is very small. Thus, the high-energy spectra of these high-efficiency GRBs can be better explained by the photosphere emission model.

2.2. Characteristics of Afterglows

In Figure 2, we show the X-ray afterglow light curves of the selected GRBs (except for GRB 990705 and GRB 000210). We find all the X-ray afterglow light curves appear as a simple power-law shape, without any plateau, steep decay (Zhang et al. 2006) or significant flare (with weak flare in the early time). In Figure 3, we show the optical afterglow light curves of 6 GRBs whose early peak can be detected. We find all the optical afterglow light curves show significant reverse shock signals. The power-law shape of the X-ray afterglow and the reverse shock in the optical afterglow are the basic predictions (Paczynski & Rhoads 1993; Mészáros & Rees 1997; Sari & Piran 1999) of the classical hot fireball model of GRB (see Appendix B2 and B3). Thus, the jet of these high-efficiency GRBs is likely to be thermal-dominated, and the radia-

tion mechanism of the prompt emission is unlikely to be the ICMART model (for Poynting-flux-dominated outflow, [Zhang & Yan 2011](#)). Also, considering the high efficiency ($\epsilon_\gamma \gtrsim 80\%$), the internal shock model ($\epsilon_\gamma \sim 10\%$, [Rees & Meszaros 1994; Kobayashi et al. 1997](#)) is unlikely. Then, the prompt emission of these GRBs is likely to be produced by the photosphere emission.

In Figure 4(a), we show the correlation of L_{iso} and Γ for the selected GRBs. The Γ is obtained by the tight $L_{\text{iso}} - E_{\text{p}} - \Gamma$ correlation ([Liang et al. 2015](#)). In Section 3.3, we find that this estimation is likely to be quite accurate for these high-efficiency GRBs with $E_{\text{p}} \propto (L_{\text{iso}})^{1/4}$. Though 4 GRBs have the detections of peak time of the optical afterglow, we do not use them to estimate the Γ because of the significant reverse shock signals. We find that Γ is tightly correlated with L_{iso} , $\Gamma \propto (L_{\text{iso}})^{0.29}$. This is well consistent with the prediction of the neutrino annihilation from the hyperaccretion disk ([Lü et al. 2012](#)), $\Gamma \propto (L_{\text{iso}})^{7/27} = (L_{\text{iso}})^{0.26}$. Then, this also supports that the jet of these GRBs is thermal-dominated.

In Figure 4(b), we show the correlation of $E_{\text{iso}}/E_{\text{k}}$ and η/Γ for the selected GRBs. Here, η represents the baryon loading, $\eta = E/Mc^2$, E and M are the injected energy and baryon mass at the outflow base, respectively. For the unsaturated acceleration case of the photosphere emission, since $T_{\text{ob}} = D \cdot T_{\text{comoving}} = \Gamma \cdot (T_0/\Gamma) = T_0$, $E_{\text{iso}} = E = \eta Mc^2$. Here, Γ is the Lorentz factor at the photosphere radius. Also, because all the thermal energy is released at the photosphere radius (no remained energy to accelerate the jet), the Lorentz factor in the afterglow phase will remain to be Γ , namely $E_{\text{k}} = \Gamma Mc^2$. So, we should have $E_{\text{iso}}/E_{\text{k}} = \eta Mc^2/\Gamma Mc^2 = \eta/\Gamma$. For the unsaturated acceleration case, R_{ph} is calculated by

$$R_{\text{ph}} = \left[\frac{\sigma_T}{6m_p c} \frac{L_{\text{iso}}}{4\pi c^2 \eta} r_0^2 \right]^{1/3}. \quad (1)$$

And, the Lorentz factor at the photosphere is given by $\Gamma = R_{\text{ph}}/r_0$. Then, along with $r_0 \sim 3.21 \times 10^8$ cm derived above and L_{iso} , we can use the Γ to obtain η for each burst. From Figure 4(b), we find the obvious linear correlation for $E_{\text{iso}}/E_{\text{k}}$ and η/Γ , and they are almost the same (except for 3 bursts). Note that we get 4 bursts to be almost the same when we take $r_0 = 3.21 \times 10^8$ cm, and then we use the offset from the best-fit $E_{\text{p}} \propto (L_{\text{iso}})^{1/4}$ relation to slightly modify r_0 for other bursts to get the other 3 bursts to be almost the same) when we take $E_{\text{k},52} = 5 * L_{\text{X},45}$ ($E_{\text{k},52} = E_{\text{k}}/10^{52}$, $L_{\text{X},45} = L_{\text{X}}/10^{45}$). This is quite close to the derivation of $E_{\text{k},52} = 3.7 * L_{\text{X},45}$ described in Section 3.1, and the slight difference is likely to come from the slight error of Γ estimated by the $L_{\text{iso}} - E_{\text{p}} - \Gamma$ correlation). This result again strongly supports the photosphere emission origin in the unsaturated acceleration regime for these high-efficiency GRBs.

2.3. Discussion for the Probability Photosphere Model and the Dissipative Photosphere Model

According to the above statements, the prompt emission of the selected high-efficiency GRBs is likely to be produced by the photosphere emission in the unsaturated acceleration regime. But noteworthy, from Table 1 we can see that the low-energy spectral index α

is quite typical (around -1), rather than very hard. This strongly supports that the photosphere emission model can produce the observed typical soft low-energy spectrum. Theoretically, the probability photosphere model (with geometric broadening) and the dissipative photosphere model (with subphotospheric energy dissipation) can both achieve this. But for the dissipative photosphere model, the $E_{\text{p}} \propto (E_{\text{iso}})^{1/4}$ relation should be violated since the inverse Compton scattering below the photosphere radius will change the photon energy (namely $T_{\text{ob}} \neq T_0$) (see Appendix A). Also, the high-energy spectrum for this model should be a power law rather than the exponential cutoff. So, the characteristics of the selected high-efficiency GRBs favor the probability photosphere model.

3. EVIDENCES IN THE LONG GRBS WITH $\epsilon_\gamma \gtrsim 50\%$ AND

$$\epsilon_\gamma \lesssim 50\%$$

3.1. $\epsilon_\gamma = 50\%$ and Maximum Γ

For the photosphere emission model, $\epsilon_\gamma \gtrsim 50\%$ and $\epsilon_\gamma \lesssim 50\%$ should correspond to the unsaturated acceleration ($\Gamma \lesssim \eta$; $E_{\text{iso}}/E_{\text{k}} = \eta Mc^2/\Gamma Mc^2 = \eta/\Gamma \gtrsim 1$) case and the saturated acceleration ($\Gamma = \eta$; $E_{\text{iso}}/E_{\text{k}} = [\eta Mc^2(R_{\text{ph}}/R_s)^{-2/3}]/\Gamma Mc^2 = (R_{\text{ph}}/R_s)^{-2/3} \lesssim 1$) case, respectively. For the $\epsilon_\gamma = 50\%$ ($R_{\text{ph}} = R_s$) case, with a fixed L_{iso} the observed Lorentz factor Γ in the afterglow phase should be maximum because of the following reason. To get $\epsilon_\gamma < 50\%$ ($R_{\text{ph}} > R_s$, $R_{\text{ph}} \propto L_{\text{iso}}/\Gamma^3$ and $R_s = \Gamma \cdot r_0$), Γ ($\Gamma = \eta$) should be smaller. Conversely, for $\epsilon_\gamma > 50\%$, η should be larger. And in this case, from Equation (13) we have $\Gamma \propto (L_{\text{iso}}/\eta)^{1/3}$, thus Γ should also be smaller. Note that this maximum Γ exists for the hot fireball, while the corresponding $\epsilon_\gamma = 50\%$ is the prediction of the photosphere emission origin for the prompt emission. The maximum Γ is given as (see the Equation 16 in [Ghirlanda et al. 2018](#) also)

$$\Gamma_{\text{max}} = \left[\frac{L_{\text{iso}} \sigma_T}{8\pi m_p c^3 r_0} \right]^{1/4}. \quad (2)$$

In Figure 6(a), we show the distribution of L_{iso} and Γ for the complete sample (62 bursts) with the detection of peak time of the early optical afterglow ([Ghirlanda et al. 2018](#)) (obtaining Γ). Obviously, except for GRB 080319B (with strong reverse shock signal) and 4 bursts (peak time is obtained from the *Fermi*/LAT light curve, and the decay slope of ~ 1.5 implies that it is likely to be produced by the radiative fireball and the Γ should be smaller by a factor of ~ 1.6 , see [Ghisellini et al. \(2010\)](#) and Appendix B4), the distribution of the maximum Γ well follows the predicted $L_{\text{iso}}^{1/4}$ correlation and only have the difference of a constant $\sim 10^{0.1}$ (1.27) from the prediction of Equation (2) (the dashed line, $r_0 \sim 3.21 \times 10^8$ cm is used based on Figure 1). Note that though the equation to calculate Γ is confirmed to act as $\Gamma \propto (E_{\text{k}})^{1/8} \cdot [T_p/(1+z)]^{-3/8}$, its constant is highly uncertain (see Table 2 in [Ghirlanda et al. \(2018\)](#)). The constant given in other works (with different methods) can be 1.7 (or 0.5) times of that used in [Ghirlanda et al. \(2018\)](#). So, the above difference (1.27) obtained by our

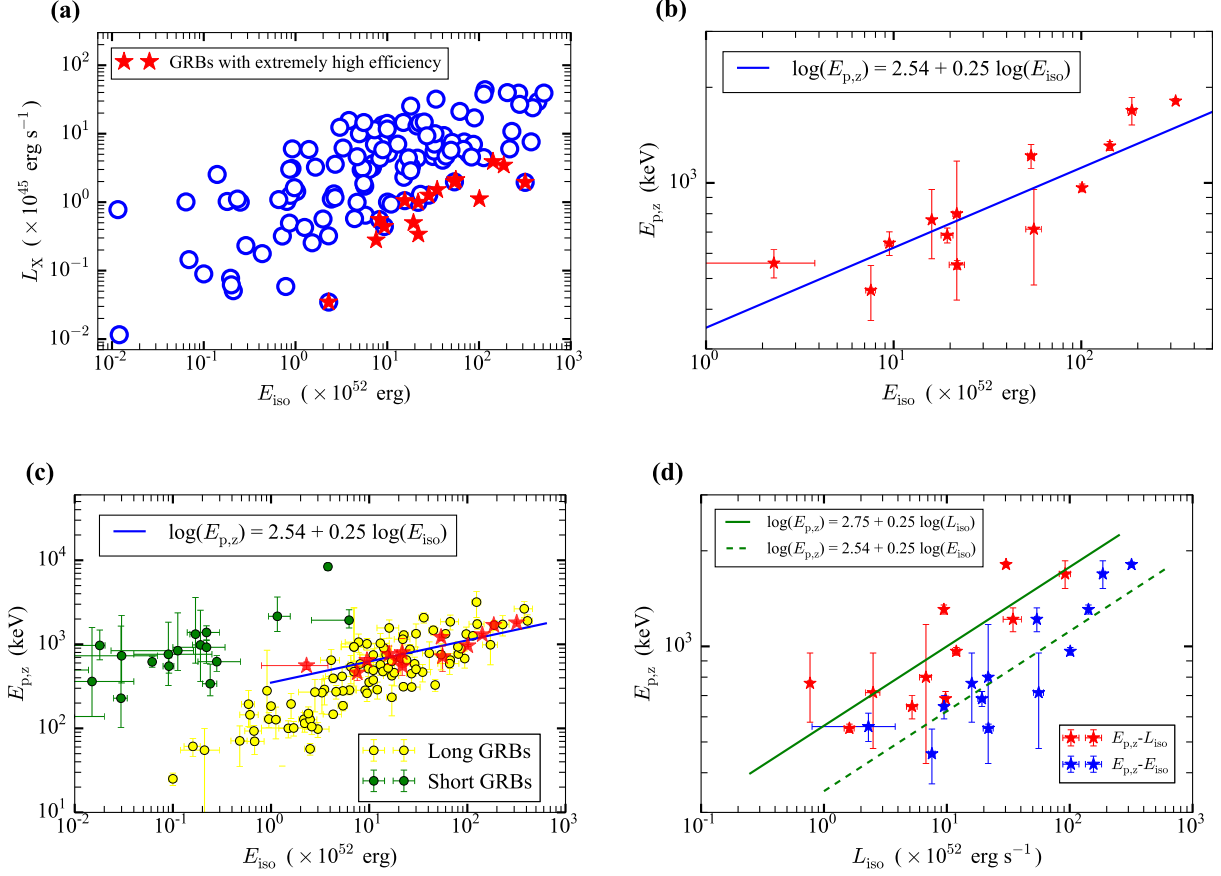


FIG. 1.— The $E_p \propto (E_{\text{iso}})^{1/4}$ and $E_p \propto (L_{\text{iso}})^{1/4}$ relations for the GRBs with the highest prompt efficiency ϵ_γ ($\epsilon_\gamma \gtrsim 80\%$). (a) The E_{iso} and calculated $L_{X,11h}$ (the late-time X-ray afterglow luminosity at 11 hours) distribution for the whole used GRB sample (117 bursts, after GRB 110213A) with redshift. The red stars with the smallest $L_{X,11h}$ represent the bursts with the highest prompt efficiency. (b) The E_p and E_{iso} distribution for the selected 15 long GRBs. The best-fit result is $\log(E_p) = 2.54 + 0.25 \log(E_{\text{iso}})$, quite consistent with the $E_p \propto (E_{\text{iso}})^{1/4}$ relation predicted by the photosphere (thermal) emission model. (c) Comparison of the E_p and E_{iso} distributions for the selected GRBs (red stars) and the large sample of long GRBs (see Figure 3 in Zhang et al. (2018b)) (yellow circles). Obviously, the dispersion for the selected GRBs is quite small relative to that for the large sample. (d) Comparison of the $E_p - L_{\text{iso}}$ distribution (red stars) and the $E_p - E_{\text{iso}}$ distribution (blue stars) for the selected GRBs. Likewise, the $E_p \propto (L_{\text{iso}})^{1/4}$ relation exists. The best-fit result is $\log(E_p) = 2.75 + 0.23 \log(L_{\text{iso}})$. And the dispersion is found to be similar to that of $E_p \propto (E_{\text{iso}})^{1/4}$.

work is reasonable and may be more accurate (since it does not strongly depend on the model assumption. If r_0 is accurate, it is likely to be accurate).

Then, we select the sample (9 bursts) with the maximum Γ (see Table 7), to check their efficiency properties. In Figure 6(b), we show the distribution of E_{iso} and $L_{X,45}$ for this sample (4 bursts with $L_{X,45}$ detection). Note that we exclude GRB 081007 due to the too small E_{iso} and GRB 080310 due to the plateau in the early optical afterglow. As expected by the photosphere emission model, all these bursts have the almost same efficiency (with $E_{\text{iso}} \propto L_X \propto E_k$). Thus, we think that the efficiency ϵ_γ for these bursts is likely to be 50% ($E_{\text{iso},52} = E_{k,52} \simeq 3.7 * L_{X,45}$). Note that, based on this the derived average efficiency ($\epsilon_\gamma \sim 33\%$ to 40%, see Figure 13) for the whole sample (117 bursts) is almost consistent with that given in other works (Lloyd-Ronning & Zhang 2004; Fan & Piran 2006; Zhang et al. 2007; D’Avanzo et al. 2012; Wygoda et al. 2016).

3.2. $E_p - E_{\text{iso}}$ Distributions and Consistent Efficiency

Based on the derivation of $E_{k,52} = 3.7 * L_{X,45}$ described above, and separated by $E_{\text{iso},52} = E_{k,52} = 3.7 * L_{X,45}$ ($\epsilon_\gamma = 50\%$) for the distribution of $E_{\text{iso},52}$ and $L_{X,45}$ in Figure 6, we get two distinguished long GRB samples ($\epsilon_\gamma \lesssim 50\%$, see Table 4; and $\epsilon_\gamma \gtrsim 50\%$, see Table 5). Note that we exclude the above high-efficiency sample ($\epsilon_\gamma \gtrsim 80\%$) and the sample with $\epsilon_\gamma = 50\%$.

For the photosphere emission model, $\epsilon_\gamma \gtrsim 50\%$ and $\epsilon_\gamma \lesssim 50\%$ should correspond to the unsaturated acceleration ($\Gamma \lesssim \eta$; $E_{\text{iso}}/E_k = \eta M c^2 / \Gamma M c^2 = \eta/\Gamma \gtrsim 1$) case and the saturated acceleration ($\Gamma = \eta$; $E_{\text{iso}}/E_k = [\eta M c^2 (R_{\text{ph}}/R_s)^{-2/3}] / \Gamma M c^2 = (R_{\text{ph}}/R_s)^{-2/3} \lesssim 1$) case, respectively. Thus, for the $\epsilon_\gamma \gtrsim 50\%$ sample, just as the above high-efficiency sample we should have the $E_p \propto (E_{\text{iso}})^{1/4}$ relation. In Figure 7(a), we show that the best-fit result for the $\epsilon_\gamma \gtrsim 50\%$ sample is $\log(E_p) = 2.47 + 0.25 \log(E_{\text{iso}})$, well consistent with the prediction of the photosphere emission model. Also, this result is almost the same as that of the above high-efficiency sample. The offset from the best-fit result is likely to be caused by a distribution of r_0 (just as

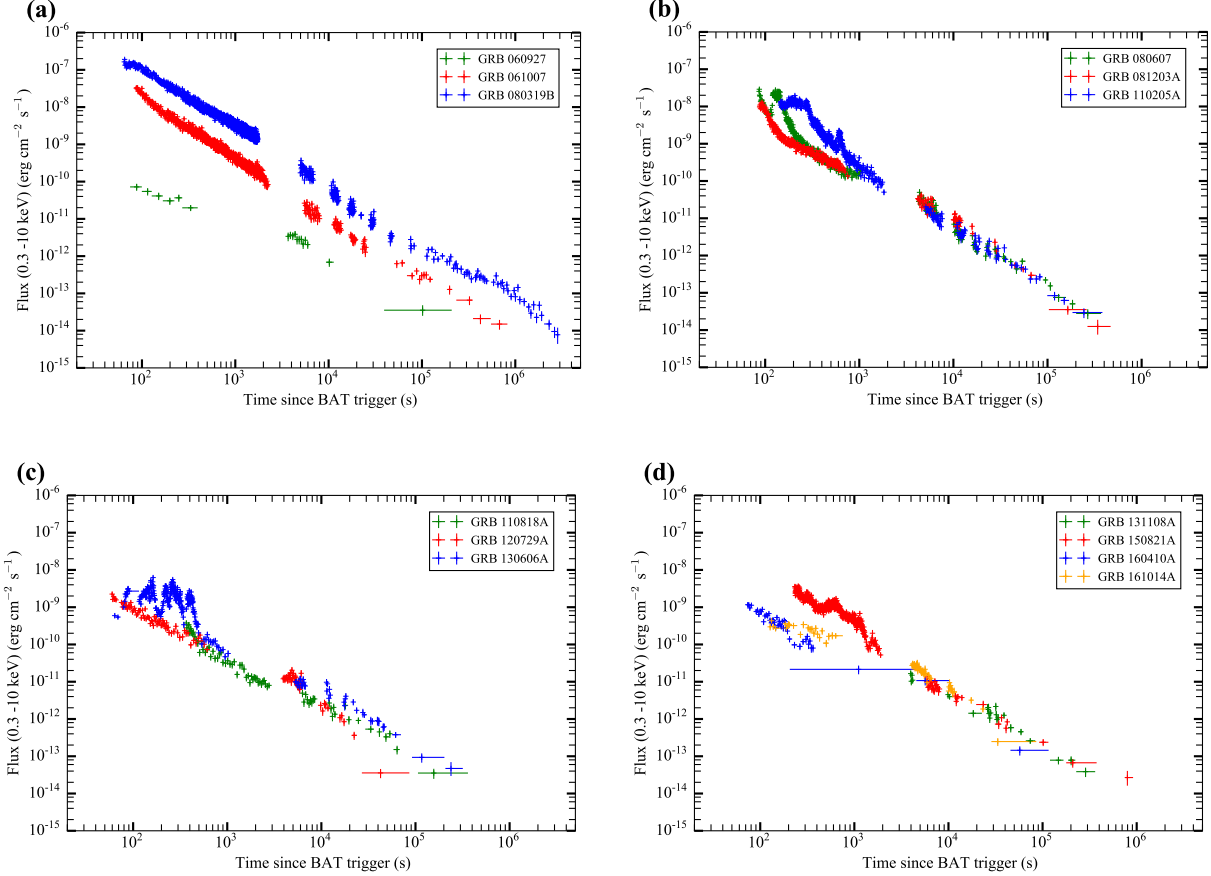


FIG. 2.— The X-ray afterglow light curves for the selected high-efficiency GRBs (except for GRB 990705 and GRB 000210). All these light curves appear as a simple power-law shape, without any plateau, steep decay or significant flare (with weak flare in the early time).

the constrained results in Pe'er et al. 2015). For the $\epsilon_\gamma \lesssim 50\%$ sample, $E_{\text{iso}} = E \cdot (R_{\text{ph}}/R_s)^{-2/3}$ and $E_p = 2.7kT_0 \cdot (R_{\text{ph}}/R_s)^{-2/3} \propto E^{1/4} \cdot (R_{\text{ph}}/R_s)^{-2/3}$. Thus, E_{iso} and E_p should both decrease by the same factor of $(R_{\text{ph}}/R_s)^{-2/3}$, compared with the distribution of $\log(E_p) = 2.54 + 0.25 \log(E_{\text{iso}})$ of the above high-efficiency sample. In Figure 7(a), we show that the up-most distribution for the $\epsilon_\gamma \lesssim 50\%$ sample is well around $\log(E_p) = 2.54 + 0.25 \log(E_{\text{iso}})$, and the best-fit result (much smaller) is $\log(E_p) = 2.31 + 0.26 \log(E_{\text{iso}})$. The decreasing of E_{iso} and E_p is more obvious, when we divide the $\epsilon_\gamma \lesssim 50\%$ sample into two sub-samples ($\epsilon_\gamma \lesssim 17\%$ and $\epsilon_\gamma \gtrsim 17\%$).

For the $\epsilon_\gamma \lesssim 50\%$ sample (saturated acceleration), we should have

$$E_{\text{iso}} = E \cdot (R_{\text{ph}}/R_s)^{-2/3} \quad (3)$$

and

$$\begin{aligned} E_p &= 2.7kT_0 \cdot (R_{\text{ph}}/R_s)^{-2/3} \\ &= 2.7k(L/4\pi r_0^2 ac)^{1/4} \cdot (R_{\text{ph}}/R_s)^{-2/3} \\ &= 2.7k(E/4\pi r_1^2 ac)^{1/4} \cdot (R_{\text{ph}}/R_s)^{-2/3} \\ &= 2.7k(4\pi r_1^2 ac)^{-1/4} \cdot E^{1/4} \cdot (R_{\text{ph}}/R_s)^{-2/3}, \end{aligned} \quad (4)$$

here $r_1^2 \simeq r_0^2 * T_{90}$. From the relation of $\log(E_p) = 2.54 + 0.25 \log(E_{\text{iso}})$, we obtain $r_1 = 8.45 \times 10^8$ cm. Then, from

Equation (3) and Equation (4), we get

$$(E_p)^4/E_{\text{iso}} = (2.7k)^4 * (4\pi r_1^2 ac)^{-1} \cdot (R_{\text{ph}}/R_s)^{-2}, \quad (5)$$

thus

$$(R_{\text{ph}}/R_s)^{-2/3} = [(E_p/2.7k)^4 * (4\pi r_1^2 ac)/E_{\text{iso}}]^{1/3}. \quad (6)$$

Also, as mentioned above we should have $E_{\text{iso}}/E_k = (R_{\text{ph}}/R_s)^{-2/3}$. In Figure 8(a), we show the distribution of E_{ratio} ($E_{\text{ratio}} = [(E_p/2.7k)^4 * (4\pi r_1^2 ac)/E_{\text{iso}}]^{1/3}$) and E_{iso}/E_k (implicitly, $E_{k,52} = 3.7 * L_{X,45}/((1+z)/2)$ is adopted) for the $\epsilon_\gamma \lesssim 50\%$ sample. They are found to be well centered around the equal-value line, and have the linear correlation. This is well consistent with the prediction of the photosphere emission model. The dispersion is likely to be caused by the estimation error for E_k (we have excluded the bursts with large E_p error of $dE_p/E_p \geq 0.2$), since many X-ray afterglow light curves are quite complex (with plateau, steep decay or significant flare). The method of using $L_{X,11h}$ to estimate E_k should only be completely correct for the X-ray afterglow with power-law shape and slope of -1 . To check the origin of the dispersion, we select the bursts with almost same E_{ratio} and E_{iso}/E_k (see Table 3). As expected, we find all these bursts (7 bursts) have a power-law X-ray afterglow light curve with slope of ~ -1 (shown in Figure 8(b) and 8(c)).

Also, according to above, for the $\epsilon_\gamma \lesssim 50\%$ sample we

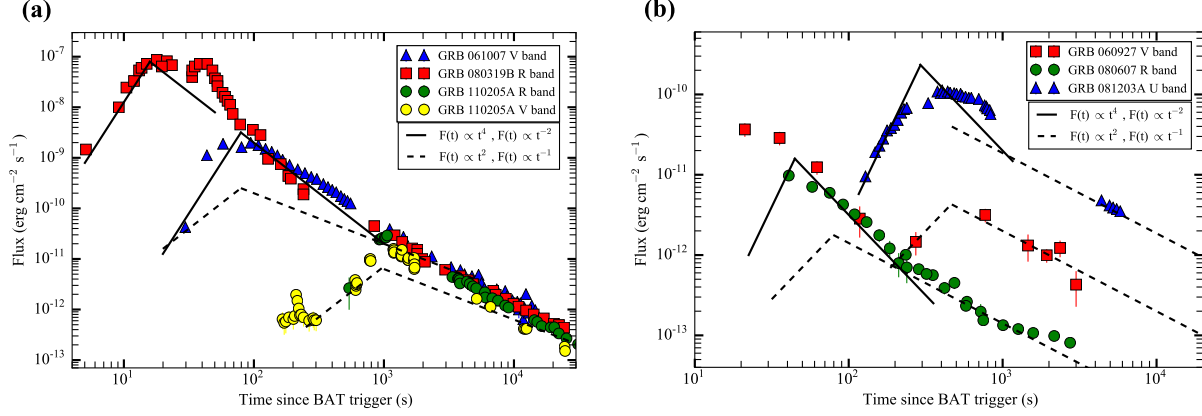


FIG. 3.— The optical afterglow light curves for 6 high-efficiency GRBs whose early peak can be detected. All these light curves show significant reverse shock signals. (a) 3 GRBs considered also to have reverse shock signals (with detections of both the rapid rise $f \gtrsim t^3$ and fall $f \sim t^{-2}$) in other works (Gao et al. 2015; Yi et al. 2020). (b) 3 GRBs with detection of only the rapid rise $f \gtrsim t^3$ or the rapid fall $f \sim t^{-2}$.

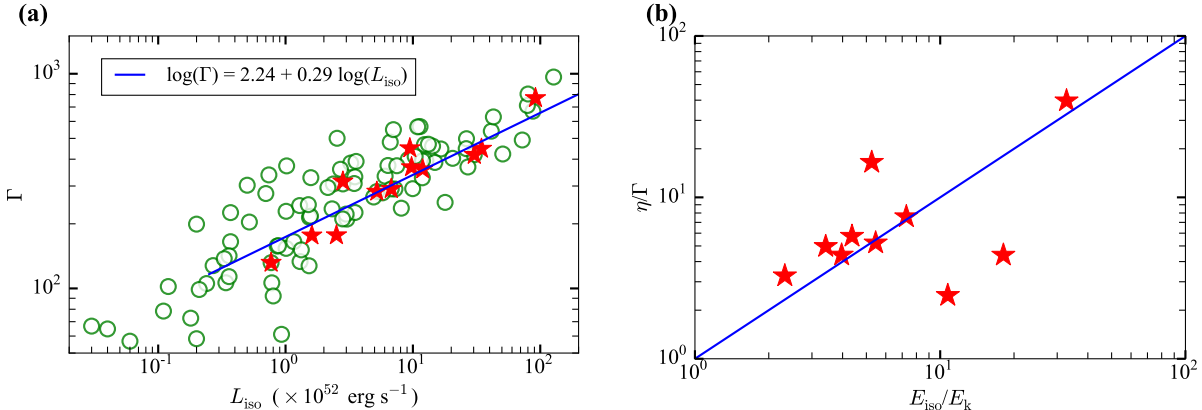


FIG. 4.— The $L_{\text{iso}} - \Gamma$ correlation and the $E_{\text{iso}}/E_{\text{k}} - \eta/\Gamma$ correlation for the selected high-efficiency GRBs. (a) The correlation of L_{iso} and Γ . Obviously, the tight correlation of $\Gamma \propto (L_{\text{iso}})^{0.29}$ (the red stars) is found, which is well consistent with the prediction of the neutrino annihilation from the hyperaccretion disk, $\Gamma \propto (L_{\text{iso}})^{7/27} = (L_{\text{iso}})^{0.26}$. Thus, the jet is likely to be thermal-dominated. (b) The correlation of $E_{\text{iso}}/E_{\text{k}}$ and η/Γ . The significant linear correlation is found, and they are almost the same when we take $E_{\text{k},52} = 5 * L_{\text{X},45}$. This is well consistent with the predicted $E_{\text{iso}}/E_{\text{k}} = \eta M c^2 / \Gamma M c^2 = \eta/\Gamma$ by the photosphere emission model in the unsaturated acceleration regime.

should have $E_{\text{ratio}} = E_{\text{iso}}/E_{\text{k}} = (R_{\text{ph}}/R_s)^{-2/3}$, here

$$R_{\text{ph}} = \frac{\sigma_T}{8\pi m_p c^3} \frac{L}{\Gamma^3}, \quad (7)$$

and $R_s = \Gamma \cdot r_0$. To check this, we select the bursts with detection of peak time of the optical afterglow (using them to estimate the Γ and thus $(R_{\text{ph}}/R_s)^{-2/3}$). Note that, since E_{ratio} and $E_{\text{iso}}/E_{\text{k}}$ is the average result for the whole duration and $(R_{\text{ph}}/R_s)^{-2/3} \propto L^{-2/3}$, we use $L = E_{\text{iso}}/T_{90}$ (rather than L_{iso}). In Figure 8(d), we show the distribution of E_{ratio} , $E_{\text{iso}}/E_{\text{k}}$ and $(R_{\text{ph}}/R_s)^{-2/3}$ for the selected sample (6 bursts). Similar to above, they are found to be well centered around the equal-value line, and have the linear correlation. Also, 1 burst has the almost same values for these three quantities and the other 5 bursts have the almost same values for two quantities of them. So, the predicted $E_{\text{ratio}} = E_{\text{iso}}/E_{\text{k}} = (R_{\text{ph}}/R_s)^{-2/3}$ by the photosphere emission model can be well reproduced.

For the $\epsilon_{\gamma} \gtrsim 50\%$ sample, similar to Figure 4(b) (for the high-efficiency GRBs), we should have $E_{\text{iso}}/E_{\text{k}} = \eta/\Gamma$. To check this, we also select the bursts with detection of peak time of the optical afterglow (using them to estimate the Γ and thus η). Note that, since $\Gamma \propto L^{1/3}$ and the derived Γ is likely to correspond to L_{iso} (maximum L), we use $L = L_{\text{iso}}$ when calculating η . In Figure 8(e), we show the distribution of $E_{\text{iso}}/E_{\text{k}}$ and η/Γ for the selected sample (7 bursts). As expected, they are found to be well centered around the equal-value line, and have the linear correlation.

The analysis results obtained above are for the sample with $L_{\text{X},11\text{h}}$ derived in this work (for GRBs after GRB 110213A). For another sample with $L_{\text{X},11\text{h}}$ presented in D'Avanzo et al. (2012) (for GRBs before GRB 110213A), we perform similar analysis and get similar results. For the $\epsilon_{\gamma} \gtrsim 50\%$ sub-sample, the E_{p} and E_{iso} distribution is also centered around $\log(E_{\text{p}}) = 2.47 + 0.25 \log(E_{\text{iso}})$ (see Figure 7(b)). For the $\epsilon_{\gamma} \lesssim 50\%$ sub-sample, the decreasing of E_{iso} and E_{p} is also obvious. Also, the dis-

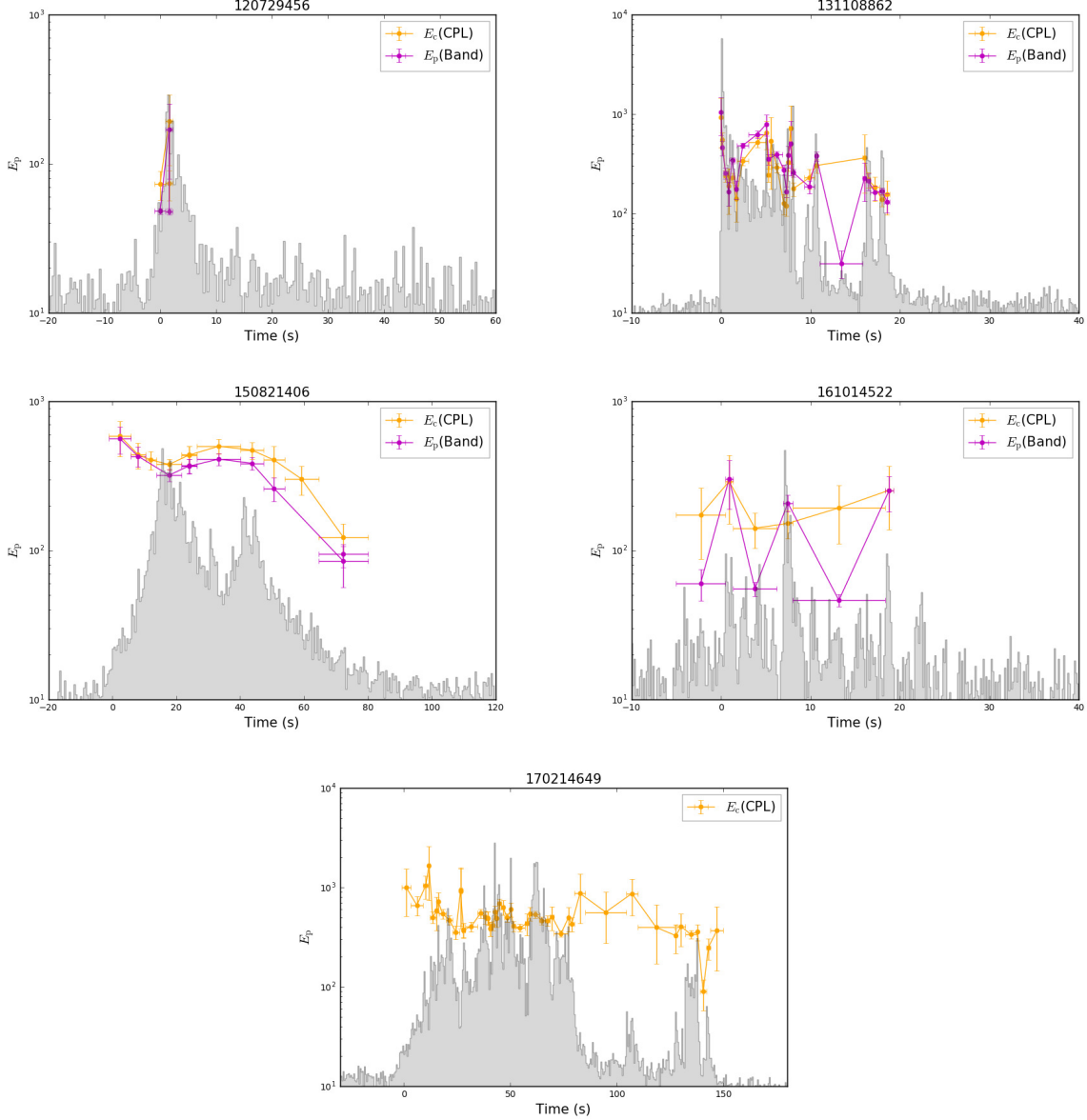


FIG. 5.— The E_p evolutions of the time-resolved spectra for 5 high-efficiency GRBs detected by *Fermi*/GBM. The E_p evolutions almost follow the evolution of the flux F , consistent with the predicted $E_p \propto F^{1/4}$ by the photosphere (thermal) emission in the unsaturated acceleration regime.

tribution for E_{ratio} and $E_{\text{iso}}/E_{\text{k}}$ are well centered around the equal-value line, and have the linear correlation (see Figure 9(a)). For the selected bursts with almost same E_{ratio} and $E_{\text{iso}}/E_{\text{k}}$ (see Table 3), all (7 bursts) show a power-law X-ray afterglow light curve with slope of ~ -1 (see Figure 9(b) and 9(c)).

3.3. The Derived Excellent $\Gamma \propto E_{\text{iso}}^{1/8} E_p^{1/2} / (T_{90})^{1/4}$ Correlation

The small burst number in Figure 8(d) is due to the small burst number of obtaining both the X-ray afterglow light curve and the detection of peak time of the early optical afterglow. Then, to further check $E_{\text{ratio}} = E_{\text{iso}}/E_{\text{k}} = (R_{\text{ph}}/R_s)^{-2/3}$ for the $\epsilon_{\gamma} \lesssim 50\%$ case, we analyze the complete sample with the detection of peak time of the early optical afterglow (obtain-

ing Γ and thus $(R_{\text{ph}}/R_s)^{-2/3}$, Ghirlanda et al. 2018) (see Table 6). Note that the used constant is 1.27 times of that given in Ghirlanda et al. (2018) (see Section 3.1). Though lacking of $E_{\text{iso}}/E_{\text{k}}$ for most bursts in the sample, considering the different distributions of E_p and E_{iso} for $\epsilon_{\gamma} \lesssim 50\%$ and $\epsilon_{\gamma} \gtrsim 50\%$, we can use the judgement of ($E_{\text{ratio}} \lesssim 0.9$) to roughly select the $\epsilon_{\gamma} \lesssim 50\%$ sub-sample. Note that we do not use the bursts without E_p value in Minaev & Pozanenko (2020) and Xue et al. (2019) due to the large E_p error, and we move 4 bursts to the $\epsilon_{\gamma} \gtrsim 50\%$ sub-sample based on their detections of $E_{\text{iso}}/E_{\text{k}}$. In Figure 10(a), we show the distribution of E_{ratio} and $(R_{\text{ph}}/R_s)^{-2/3}$ for the selected $\epsilon_{\gamma} \lesssim 50\%$ sub-sample (24 bursts). This distribution is roughly centered around the equal-value line, and have the linear correlation. After modifying the Γ or E_p based on Fig-

TABLE 1
THE OBSERVED QUANTITIES FOR THE BURSTS WITH EXTREMELY HIGH EFFICIENCY ($\epsilon_\gamma \gtrsim 80\%$).

GRB	z	L_{iso} ($10^{52} \text{ erg s}^{-1}$)	E_{iso} (10^{52} erg)	$L_{\text{X,11}}$ ($10^{45} \text{ erg s}^{-1}$)	Efficiency	$E_{p,z}$ (keV)	α	β	best-fitted model
990705 ^a	0.8424	1.61 ± 0.15^c	21.8 ± 0.8	1.14	$0.83 (0.99^f)$	551 ± 17	-0.72 ± 0.03	-2.68 ± 0.15^e	
000210 ^a	0.8463	9.76 ± 0.5^c	19.3 ± 0.5	1.67	$0.74 (0.97^f)$	687^{+39}_{-37}			
060927 ^b	5.47	10.8 ± 0.8	7.56 ± 0.46	0.28	0.96	459 ± 90	-0.81 ± 0.36		
061007 ^b	1.261	10.9 ± 0.9	101 ± 1.4	1.11	0.97	965 ± 27	-0.75 ± 0.02	-2.79 ± 0.09	
080319B ^b	0.9382	10.2 ± 0.9	142 ± 3	3.90	0.91	1307 ± 43	-0.86 ± 0.01	-3.59 ± 0.45	
080607 ^b	3.0363	225.9 ± 45.3	186 ± 10	3.46	0.97	1691 ± 169	-1.08 ± 0.06		
081203A ^b	2.05	2.82 ± 0.19	35.0 ± 12.8	1.52	0.90	1541 ± 756	-1.29 ± 0.14		
110205A ^b	2.22	2.51 ± 0.34	55.9 ± 5.3	2.12	0.92	715 ± 238	-1.52 ± 0.14		
110818A ^c	3.36	6.76 ± 0.76	21.7 ± 1.02	0.99	0.93	799.45 ± 371.90	-1.19 ± 0.08		COM ^d
120729A ^a	0.80		2.3 ± 1.5	0.034	0.94	559 ± 57			
130606A ^a	5.913		28.3 ± 5.2	1.26	0.95	2032^{+622}_{-346}	-1.14 ± 0.15		COM ^e
131108A ^a	2.40	26.22 ± 0.6^c	54 ± 2.4	1.98	0.93	1217^{+105}_{-88}	-1.16 ± 0.07		COM ^e
150821A ^a	0.755	0.77 ± 0.03^c	15.5 ± 1.2	1.05	0.78	765^{+188}_{-126}	-1.52 ± 0.05		COM ^e
160410A ^{a,s}	1.717		9.3 ± 1.8	0.44	0.89	3853^{+1429}_{-973}	-0.71 ± 0.20		COM ^e
161014A ^c	2.823	5.21 ± 0.52	9.49 ± 0.50	0.55	0.90	646.18 ± 55.13	-0.76 ± 0.08		COM ^d
170214A ^a	2.53	30.32 ± 0.85^c	318.43 ± 0.21	1.94	0.99	1810 ± 34	-0.98 ± 0.01	-2.51 ± 0.10^d	
130606A ^a	5.913		28.3 ± 5.2	1.26	0.95	2032^{+622}_{-346}	-1.14 ± 0.15		COM ^e

^a E_{iso} and $E_{p,z}$ are taken from Minaev & Pozanenko (2020). ^b E_{iso} , $E_{p,z}$, L_{iso} , α and β are taken from Nava et al. (2012). ^c E_{iso} , $E_{p,z}$ and L_{iso} (or L_{iso} alone) are taken from Xue et al. (2019). ^d The spectral analysis results from Fermi GBM Burst Catalog (von Kienlin et al. 2020). ^e The spectral analysis results from Konus/Wind Burst Catalog (Tsvetkova et al. 2017). ^f The extremely-high efficiency claimed in Lloyd-Ronning & Zhang (2004). ^s The short GRB.

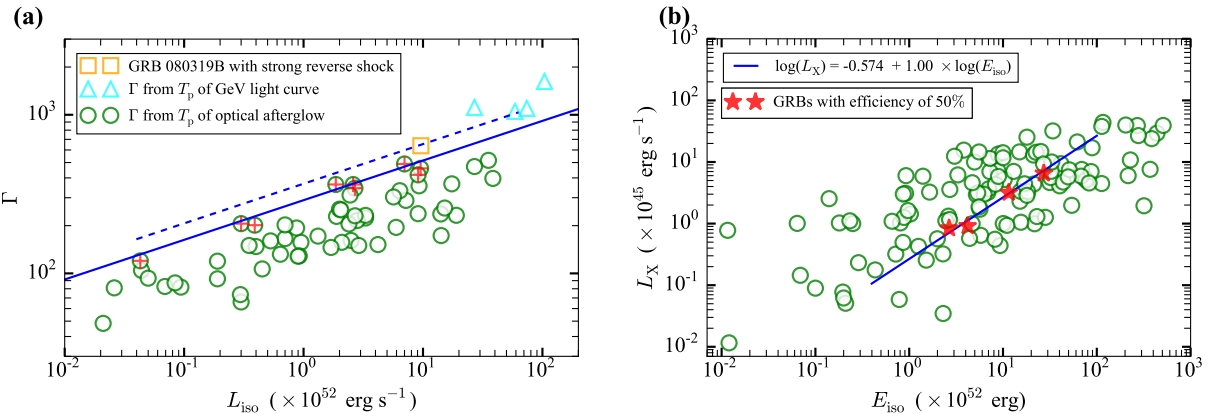


FIG. 6.— The L_{iso} – Γ and E_{iso} – $L_{\text{X,45}}$ distributions for the $\epsilon_\gamma = 50\%$ sample. (a) The distribution of L_{iso} and Γ for the complete sample (62 bursts) with the detection of T_p . We select the sample (9 bursts, marked by the red plus) with the maximum Γ (for fixed L_{iso}), to check whether their efficiency is 50% as predicted by the photosphere emission model. (b) The distribution of E_{iso} and $L_{\text{X,45}}$ for the selected sample with the maximum Γ (4 bursts with $L_{\text{X,45}}$ detection, red stars). It is found that, all these bursts have the almost same efficiency (with $E_{\text{iso}} \propto L_{\text{X}} \propto E_{\text{k}}$). Thus, we think that the efficiency ϵ_γ for these bursts is likely to be 50% ($E_{\text{iso},52} = E_{\text{k},52} \simeq 3.7 * L_{\text{X},45}$).

ure 8(d) (using $E_{\text{ratio}} = E_{\text{iso}}/E_{\text{k}} = (R_{\text{ph}}/R_s)^{-2/3}$) for the 6 bursts there, in Figure 10(b) we show the distributions of E_{ratio} and $(R_{\text{ph}}/R_s)^{-2/3}$ for the two sub-samples with smaller E_p error ($dE_p/E_p \leq 0.2$) and larger E_p error ($dE_p/E_p \geq 0.2$). Obviously, for the sub-sample with smaller E_p error, the values of E_{ratio} and $(R_{\text{ph}}/R_s)^{-2/3}$ are almost the same. Note that we decrease the Γ of GRB 090926A by a factor of 1.6, since its peak time is obtained from the LAT light curve and the decay slope of ~ 1.5 implies that it is likely to be produced by the radiative fireball (Ghisellini et al. 2010). And, for the large offset in Figure 10(b) (the upper offset), we check its (GRB 090618) optical afterglow light curve and find that the reverse shock signal is significant, thus overestimating the Γ and $(R_{\text{ph}}/R_s)^{-2/3}$.

As shown in Figure 10(b), we have $E_{\text{ratio}} =$

$$(R_{\text{ph}}/R_s)^{-2/3}$$

$$[(E_p/2.7k)^4 * (4\pi r_1^2 ac)/E_{\text{iso}}]^{1/3} = \left(\frac{\sigma_T}{8\pi m_p c^3} \frac{E_{\text{iso}}/T_{90}}{\Gamma^4 \cdot r_0} \right)^{-2/3} \quad (8)$$

Thus, we can use the quantities of prompt emission (E_{iso} , E_p and T_{90}) to estimate the Lorentz factor Γ , just as the obtained $\Gamma = 10^{3.33} L_{\text{iso}}^{0.46} E_p^{-0.43}$ from the statistic fitting in Liang et al. (2015). Based on Equation (8), we derive

$$\Gamma \propto E_{\text{iso}}^{1/8} E_p^{1/2} / (T_{90})^{1/4} \quad (9)$$

In Figure 10(c), we show the comparison of the Γ obtained from the optical afterglow (for all 62 bursts in Ghirlanda et al. 2018) and the Γ obtained from the prompt emission (orange triangles for

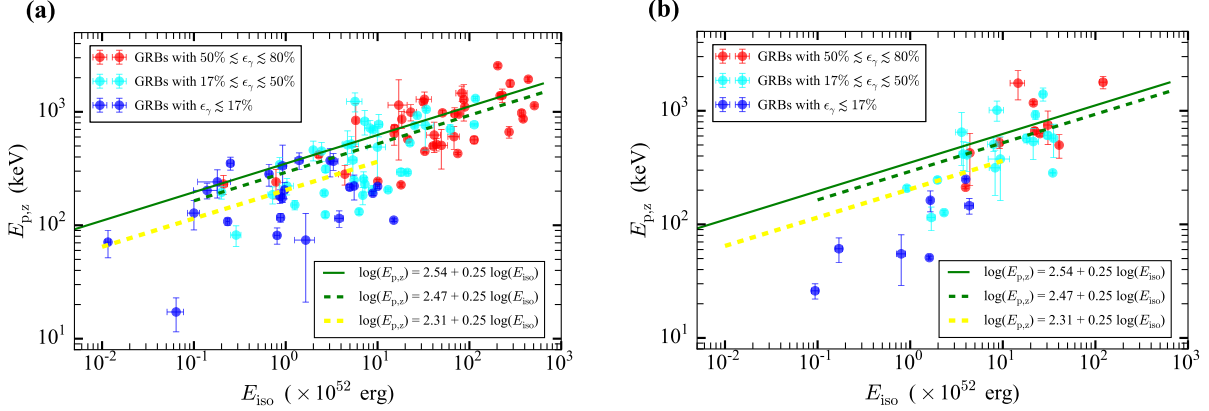


FIG. 7.— The different distributions for E_p and E_{iso} of the two distinguished samples ($\epsilon_\gamma \gtrsim 50\%$ and $\epsilon_\gamma \lesssim 50\%$) for the long GRBs. (a) The E_p and E_{iso} distribution for the bursts after GRB 110213A (117 bursts, with $L_{X,11h}$ derived in this work). For the $\epsilon_\gamma \gtrsim 50\%$ (red circles) sample, the best-fit result is $\log(E_p) = 2.47 + 0.25 \log(E_{\text{iso}})$, well consistent with the predicted $E_p \propto (E_{\text{iso}})^{1/4}$ by the photosphere emission model. For the $\epsilon_\gamma \lesssim 50\%$ (blue and cyan circles) sample, the up-most distribution is found well around $\log(E_p) = 2.54 + 0.25 \log(E_{\text{iso}})$, and the best-fit result is $\log(E_p) = 2.31 + 0.26 \log(E_{\text{iso}})$, quite below that. (b) The E_p and E_{iso} distribution for the bursts before GRB 110213A (46 bursts, with $L_{X,11h}$ given in D'Avanzo et al. 2012). The different distributions for E_p and E_{iso} of the two distinguished samples ($\epsilon_\gamma \gtrsim 50\%$ and $\epsilon_\gamma \lesssim 50\%$) are also found, which are similar to the distributions for the bursts after GRB 110213A.

$\Gamma = 10^{3.33} L_{\text{iso}}^{0.46} E_p^{-0.43}$ and blue circles for $\Gamma = 17 \cdot E_{\text{iso}}^{1/8} E_p^{1/2} / (T_{90})^{1/4}$. Obviously, using these two correlations we can give an approximate estimation for Γ , both. Furthermore, the Equation (9) derived in our work from the photosphere emission model can give a better estimation for Γ (with smaller reduced χ^2).

3.3.1. $T_p/(1+z) \propto [E_p/(T_{90})^{1/2}]^{-4/3}$ test

Note that when using the optical afterglow to obtain Γ , we have

$$\begin{aligned} \Gamma &\propto (E_k)^{1/8} \cdot [T_p/(1+z)]^{-3/8} \\ &\propto (E_{\text{iso}}/\epsilon_\gamma)^{1/8} \cdot [T_p/(1+z)]^{-3/8}, \end{aligned} \quad (10)$$

here ϵ_γ is taken as 0.2, and T_p is the peak time of the optical afterglow. Then, if the Equation (9) is correct, combining Equation (9) and Equation (10) we should have

$$T_p/(1+z) \propto [E_p/(T_{90})^{1/2}]^{-4/3}. \quad (11)$$

To test this correlation, in Figure 10(d) we show the distribution of $E_p/(T_{90})^{1/2}$ and $T_p/(1+z)$ for 35 bursts (we delect 7 bursts with $dE_p/E_p \geq 0.2$ and 5 bursts with LAT light curve, and we modify the E_p or T_p for 5 bursts based on Figure 8(d)). Just as predicted, this distribution shows the linear correlation with the slope of $\sim -4/3$, and is consistent with $T_p/(1+z) \propto (E_p)^{-1.25}$ presented in Table 1 of Ghirlanda et al. (2018). So, the Equation (9) is likely to be correct.

Besides, from Figure 10(d) we can see that the T_p for the sub-sample of $\epsilon_\gamma \gtrsim 50\%$ is a bit larger than that for $\epsilon_\gamma \lesssim 50\%$, though both satisfying the $T_p/(1+z) \propto [E_p/(T_{90})^{1/2}]^{-4/3}$ correlation. This means that the Equation (9) should have slightly different constants for the $\epsilon_\gamma \lesssim 50\%$ case and the $\epsilon_\gamma \gtrsim 50\%$ case. Actually, for the $\epsilon_\gamma \lesssim 50\%$ case, from $E_{\text{ratio}} = (R_{\text{ph}}/R_s)^{-2/3}$ we obtain

$$\Gamma = 19.67 \cdot E_{\text{iso}}^{1/8} E_p^{1/2} / (T_{90})^{1/4}. \quad (12)$$

For the $\epsilon_\gamma \gtrsim 50\%$ case, from Equation (1) we have

$$\begin{aligned} \Gamma &= R_{\text{ph}}/r_0 = \left[\frac{\sigma_T}{6m_p c} \frac{L_{\text{iso}}}{4\pi c^2 \eta} r_0^2 \right]^{1/3} / r_0 \\ &= \left[\frac{\sigma_T}{6m_p c} \frac{L_{\text{iso}}}{4\pi c^2 \eta r_0} \right]^{1/3}. \end{aligned} \quad (13)$$

Thus, $L_{\text{iso}} \propto E_{\text{iso}}/(T_{90}) \propto \eta \cdot \Gamma^3$. Combined with $E_{\text{iso}}/E_k = \eta M c^2 / \Gamma M c^2 = \eta/\Gamma$, we have $1/T_{90} \propto (1/E_k) \cdot \Gamma^4$, namely $E_k \propto \Gamma^4 \cdot T_{90}$. Putting this into $\Gamma \propto (E_k)^{1/8} \cdot [T_p/(1+z)]^{-3/8}$, we obtain $\Gamma \propto \Gamma^{1/2} \cdot (T_{90})^{1/8} \cdot [T_p/(1+z)]^{-3/8}$, namely $\Gamma^{1/2} \cdot (T_{90})^{-1/8} \propto [T_p/(1+z)]^{-3/8}$. From Figure 11(a) (discussed in the following), we have $\Gamma \propto E_p/(T_{90})^{1/4}$. So, the same as the $\epsilon_\gamma \lesssim 50\%$ case, $E_p^{1/2} / (T_{90})^{1/4} \propto [T_p/(1+z)]^{-3/8}$ is obtained. This means that the Equation (9) is also available for the $\epsilon_\gamma \gtrsim 50\%$ case. After considering the constants, we get

$$\Gamma = 16.75 \cdot E_{\text{iso}}^{1/8} E_p^{1/2} / (T_{90})^{1/4}. \quad (14)$$

The smaller constant (16.75) is consistent with the larger T_p in Figure 10(d). In Figure 10(e), we show the derived Γ using the Equation (12) and the Equation (14), and find that the distribution for the $\epsilon_\gamma \lesssim 50\%$ case is better (more symmetric) than that in Figure 10(c). Note that the above calculation of Γ , using the optical afterglow, has assumed the efficiency of $\sim 20\%$ (namely $E_k = 5 \cdot E_{\text{iso}}$). In fact, when calculating Γ we should modify the E_k based on the real efficiency (η/Γ). For the $\epsilon_\gamma \gtrsim 50\%$ case, we typically have $\eta/\Gamma \sim 3.5$ (see Figure 11(a) and Figure 13). Thus, the constant ~ 16.75 should be ~ 1.4 times smaller.

3.3.2. $\Gamma = 10^{-0.1} \cdot E_p / (T_{90})^{1/4}$ correlation

As shown in Figure 7(a), we have $E_p \propto (E_{\text{iso}})^{1/4}$ for both the $\epsilon_\gamma \gtrsim 50\%$ case (smaller dispersion) and the

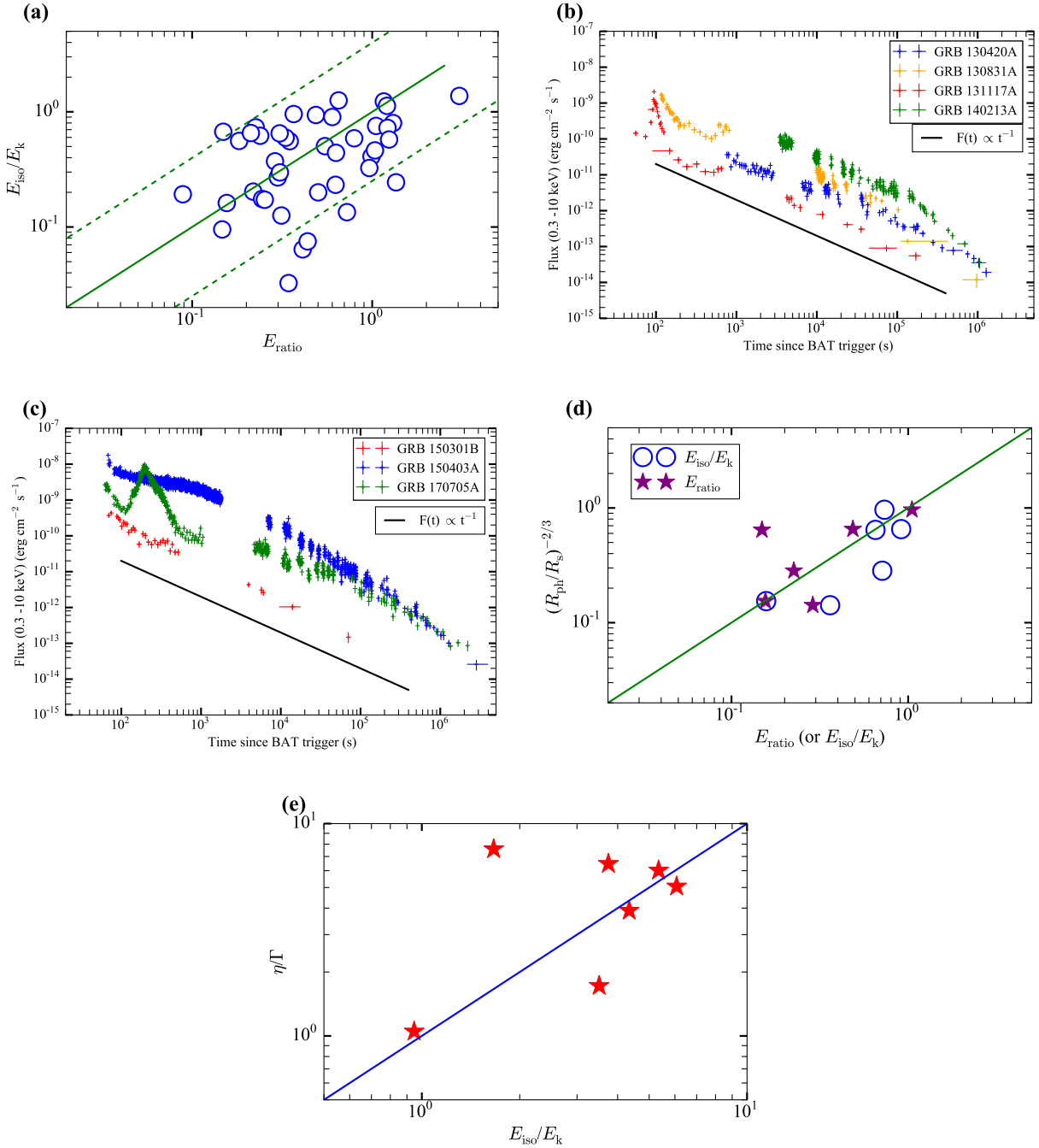


FIG. 8.— The similar observed efficiency (with E_{iso}/E_k from the X-ray afterglow) and theoretical predicted efficiency (from the prompt emission or the optical afterglow) by the photosphere emission model for the bursts after GRB 110213A. (a) The distribution of E_{ratio} ($E_{\text{ratio}} = [(E_p/2.7k)^4 * (4\pi r_p^2 ac)/E_{\text{iso}}]^{1/3}$, from the prompt emission) and E_{iso}/E_k for the $\epsilon_{\gamma} \lesssim 50\%$ sample. They are found to be well centered around the equal-value line, and have the linear correlation. The dispersion is likely to be caused by the estimation error for E_k , since many X-ray afterglow light curves are not the power law with slope of -1 . (b) and (c) The X-ray afterglow light curves for the bursts (7 bursts) with almost same E_{ratio} and E_{iso}/E_k (see Table 3). We find all these light curves do have the power-law shape with slope of ~ -1 . (d) The distribution of E_{ratio} , E_{iso}/E_k and $(R_{\text{ph}}/R_s)^{-2/3}$ for the sample (6 bursts) with detections of peak time of the optical afterglow (to estimate the Γ and thus $(R_{\text{ph}}/R_s)^{-2/3}$). It is found that, 1 bursts have the almost same values for these three quantities and the other 5 bursts have the almost same values for two quantities of them. (e) The consistent efficiency from observation (with E_{iso}/E_k) and the prediction of photosphere emission model (with η/Γ) for the $\epsilon_{\gamma} \gtrsim 50\%$ sample with detections of peak time of the optical afterglow (7 bursts).

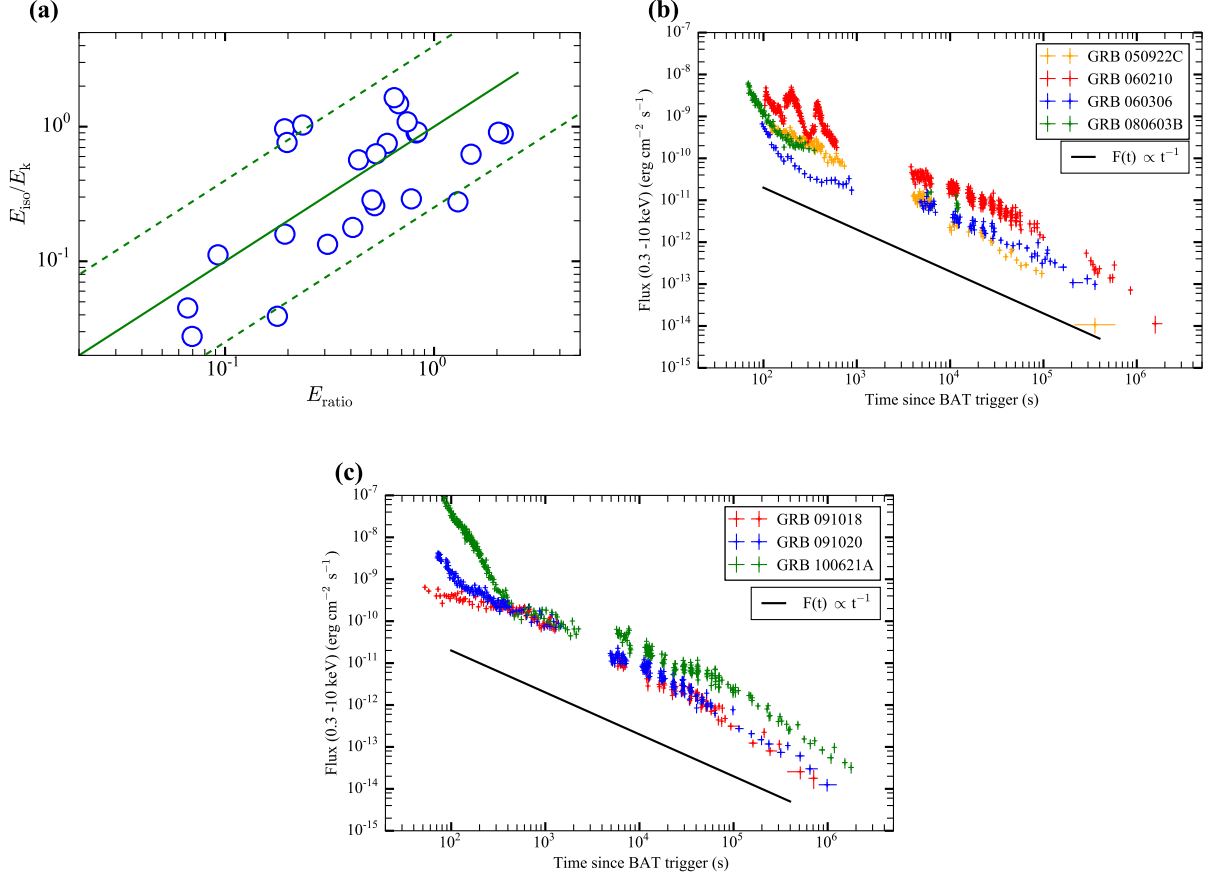


FIG. 9.— The similar observed efficiency (with $E_{\text{iso}}/E_{\text{k}}$ from the X-ray afterglow) and theoretical predicted efficiency (from the prompt emission) for the bursts before GRB 110213A. (a) The distribution of E_{ratio} and $E_{\text{iso}}/E_{\text{k}}$ for the $\epsilon_{\gamma} \lesssim 50\%$ sample. They are found to be well centered around the equal-value line, and have the linear correlation. (b) and (c) The X-ray afterglow light curves for the bursts (7 bursts) with almost same E_{ratio} and $E_{\text{iso}}/E_{\text{k}}$ (see Table 3). We find all these light curves do have the power-law shape with slope of ~ -1 .

$\epsilon_{\gamma} \lesssim 50\%$ case (larger dispersion). Then, with the Equation (9) we should obtain $\Gamma \propto E_{\text{p}}/(T_{90})^{1/4}$. On the other hand, from Figure 4(a) and Figure 6(a) we have approximately $\Gamma \propto (L_{\text{iso}})^{1/4}$, thus $\Gamma \propto E_{\text{p}}/(T_{90})^{1/4}$ is also likely to be got. In Figure 11(a), we do find this tight correlation of

$$\Gamma = 10^{-0.1} \cdot E_{\text{p}}/(T_{90})^{1/4} \quad (15)$$

for the $\epsilon_{\gamma} \gtrsim 50\%$ case (with $L_{\text{X,11h}}$ detection). Note that the E_{p} here is re-derived from the $\log(E_{\text{p}}) = 2.54 + 0.25 \log(E_{\text{iso}})$ correlation (using the E_{iso}), since the observed E_{p} with offset from the above line is likely to arise from the different r_0 (actually $E_{\text{p}} \propto (E_{\text{iso}}/r_0^2)^{1/4}$) or the error of E_{p} . Besides, we modify the Γ (using $E_{\text{iso}}/E_{\text{k}}$, mainly for 3 bursts) based on Figure 8(e). In Figure 11(a), we also show the distributions for $E_{\text{p}} - \Gamma$ and $E_{\text{p}} - \eta$, here η is obtained by $\eta/\Gamma = E_{\text{iso}}/E_{\text{k}}$. It is obvious that there is a tight correlation of $E_{\text{p}} \propto \eta$ for the sub-sample (5 bursts) with higher efficiency. This means $\eta \propto (E_{\text{iso}})^{1/4}$, which is well consistent with the prediction of the neutrino annihilation from the hyperaccretion disk (for the hot fireball).

For the $\epsilon_{\gamma} \lesssim 50\%$ case, since $(E_{\text{p}}/E_{\text{ratio}}) \propto (E_{\text{iso}}/E_{\text{ratio}})^{1/4}$ and $\Gamma \propto (L_{\text{iso}}/E_{\text{ratio}})^{1/4}$ we should have $\Gamma \propto (E_{\text{p}}/E_{\text{ratio}})/(T_{90})^{1/4}$. From Figure 11(b) we do

find this correlation, which is also in line with that for the $\epsilon_{\gamma} \gtrsim 50\%$ case. Note that we modify the E_{p} or Γ based on Figure 8(d). In Figure 11(c) we show the distribution of $\Gamma - E_{\text{p}}/(T_{90})^{1/4}$ for the large Γ sample (47 bursts) in Ghirlanda et al. (2018). Note that for the $\epsilon_{\gamma} \gtrsim 50\%$ case the E_{p} is re-derived from the $\log(E_{\text{p}}) = 2.54 + 0.25 \log(E_{\text{iso}})$ correlation (using the E_{iso}), and for the $\epsilon_{\gamma} \lesssim 50\%$ case the E_{p} is re-derived from $E_{\text{p}}/E_{\text{ratio}}$. For the $\epsilon_{\gamma} \gtrsim 50\%$ case, when calculating Γ we modify the E_{k} based on the original η/Γ . Obviously, we find the distribution of Γ and $E_{\text{p}}/(T_{90})^{1/4}$ is well centered around $\Gamma = 10^{-0.1} \cdot E_{\text{p}}/(T_{90})^{1/4}$ and shows a linear correlation.

3.3.3. Consistency of our $\Gamma \propto E_{\text{iso}}^{1/8} E_{\text{p}}^{1/2}/(T_{90})^{1/4}$ correlation and the $\Gamma = 10^{3.33} L_{\text{iso}}^{0.46} E_{\text{p}}^{-0.43}$ correlation

For the better sample (35 bursts) in Figure 10(d), in Figure 12(a) we replot the comparison of the Γ obtained from the optical afterglow and the Γ obtained from the prompt emission (orange triangles for $\Gamma = 10^{3.33} L_{\text{iso}}^{0.46} E_{\text{p}}^{-0.43}$ and blue circles for $\Gamma \propto E_{\text{iso}}^{1/8} E_{\text{p}}^{1/2}/(T_{90})^{1/4}$). For the $\epsilon_{\gamma} \gtrsim 50\%$ sub-sample (17 bursts) and the $\epsilon_{\gamma} \lesssim 50\%$ sub-sample (18 bursts), we use the derived different constants. Obviously, the Equation (9) derived in our work gives a much better estimation

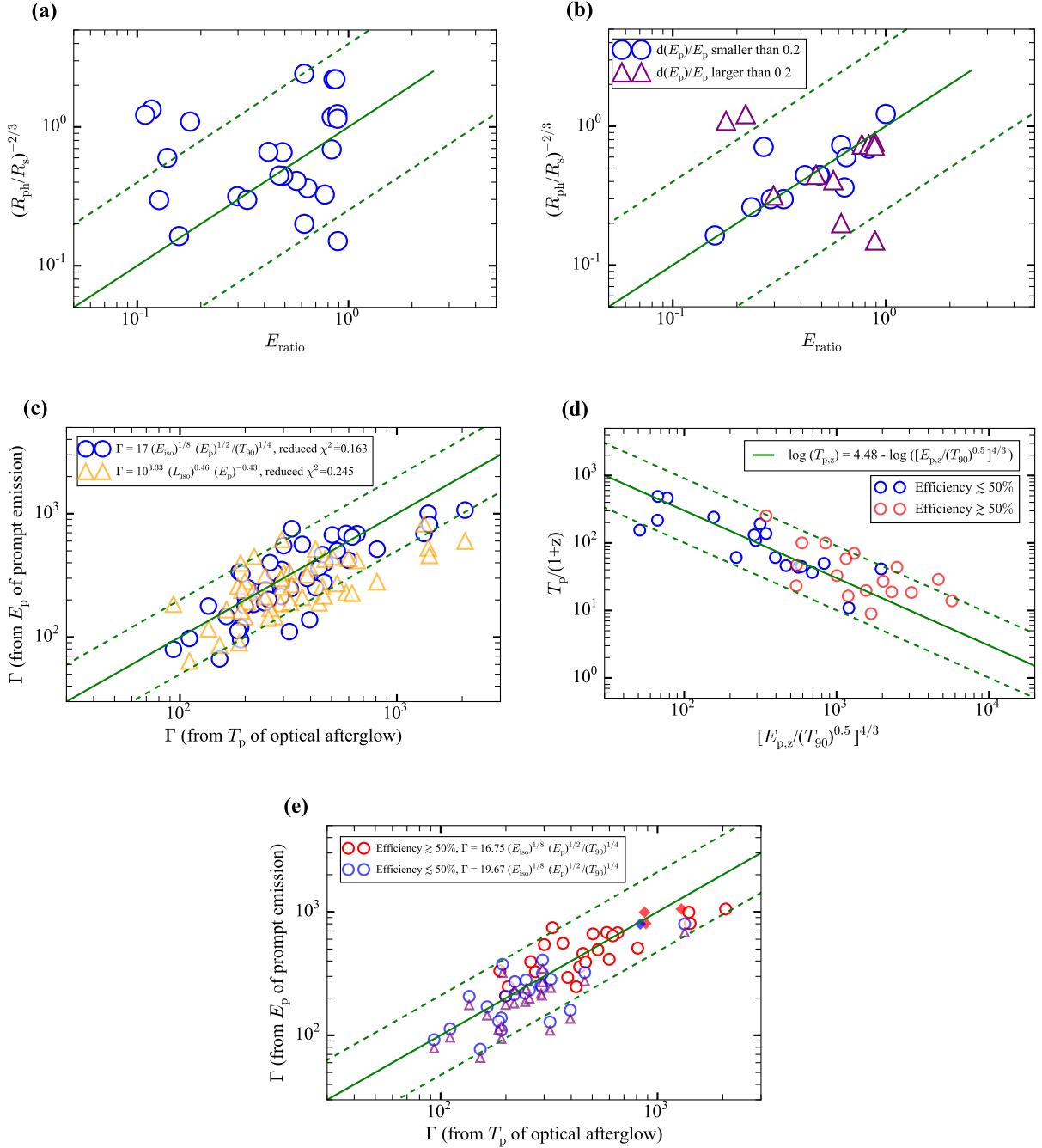


FIG. 10.— The tight correlation of $\Gamma \propto E_{\text{iso}}^{1/8} E_p^{1/2} / (T_{90})^{1/4}$ to estimate Γ , we derived based on the same efficiency of E_{ratio} and $(R_{\text{ph}}/R_s)^{-2/3}$ in the $\epsilon_{\gamma} \lesssim 50\%$ case. (a) The distribution of E_{ratio} and $(R_{\text{ph}}/R_s)^{-2/3}$ for the selected $\epsilon_{\gamma} \lesssim 50\%$ sample (based on $E_{\text{ratio}} \leq 0.9$, 24 bursts). (b) The distributions of E_{ratio} and $(R_{\text{ph}}/R_s)^{-2/3}$ for the two sub-samples with smaller E_p error ($dE_p/E_p \leq 0.2$, blue circles) and larger E_p error ($dE_p/E_p \geq 0.2$, purple triangles). (c) The comparison of the Γ obtained from the optical afterglow (for all 62 bursts in Ghirlanda et al. 2018) and the Γ obtained from the prompt emission (orange triangles for $\Gamma = 10^{3.33} L_{\text{iso}}^{0.46} E_p^{-0.43}$ and blue circles for $\Gamma = 17 \cdot E_{\text{iso}}^{1/8} E_p^{1/2} / (T_{90})^{1/4}$). (d) The distribution of $[E_p / (T_{90})^{1/2}]^{4/3}$ and $T_p / (1+z)$ for 35 bursts. (e) The slightly different constants for the $\epsilon_{\gamma} \lesssim 50\%$ case and the $\epsilon_{\gamma} \gtrsim 50\%$ case.

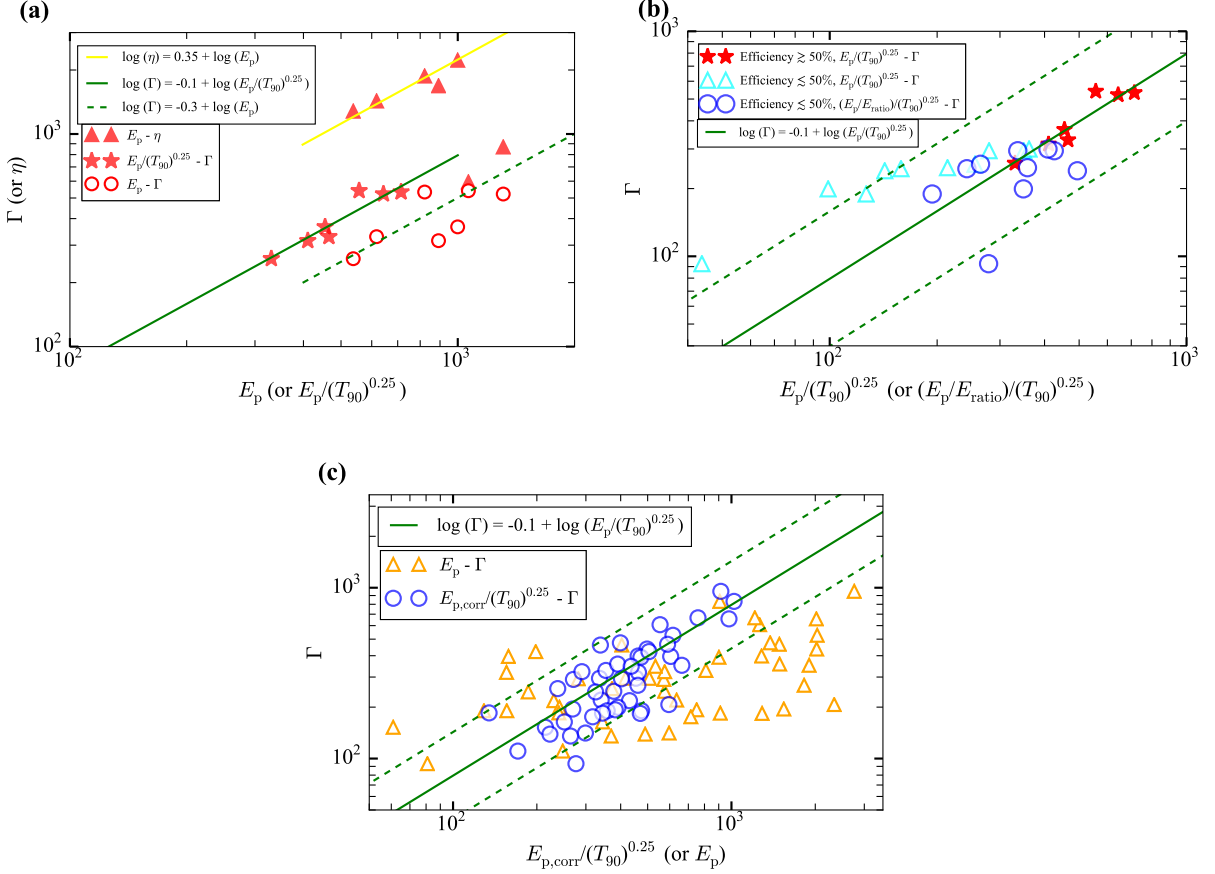


FIG. 11.— The tight correlation of $\Gamma \propto E_p/(T_{90})^{1/4}$, predicted by $\Gamma \propto E_{\text{iso}}^{1/8} E_p^{1/2}/(T_{90})^{1/4}$ and $E_p \propto (E_{\text{iso}})^{1/4}$. (a) The distributions of $E_p - \Gamma$ (red circles), $E_p - \eta$ (red triangles) and $E_p/(T_{90})^{1/4} - \Gamma$ (red stars) for the selected $\epsilon_\gamma \gtrsim 50\%$ sample with T_p detection (7 bursts in Figure 8(e)). It is obvious that, the tight correlations of $\Gamma = 10^{-0.1} \cdot E_p/(T_{90})^{1/4}$ and $E_p \propto \eta$ (for the 5 bursts with higher efficiency, thus $\eta \propto (E_{\text{iso}})^{1/4}$) are found. (b) The distributions of $(E_p/E_{\text{ratio}})/(T_{90})^{1/4} - \Gamma$ (blue circles) and $E_p/(T_{90})^{1/4} - \Gamma$ (cyan triangles) for the selected $\epsilon_\gamma \lesssim 50\%$ sample with T_p detection. The tight correlation of $(E_p/E_{\text{ratio}})/(T_{90})^{1/4} \propto \Gamma$ is found, which is in line with the $E_p/(T_{90})^{1/4} \propto \Gamma$ correlation for the $\epsilon_\gamma \gtrsim 50\%$ case. (c) The distribution of $\Gamma - E_p/(T_{90})^{1/4}$ (blue circles) for the large sample with Γ (47 bursts) in Ghirlanda et al. (2018). For the $\epsilon_\gamma \gtrsim 50\%$ case the E_p is re-derived from the $\log(E_p) = 2.54 + 0.25 \log(E_{\text{iso}})$ correlation (using the E_{iso}), and for the $\epsilon_\gamma \lesssim 50\%$ case the E_p is re-derived from E_p/E_{ratio} . Obviously, we find the distribution of Γ and $E_p/(T_{90})^{1/4}$ is well centered around $\Gamma = 10^{-0.1} \cdot E_p/(T_{90})^{1/4}$ and have a linear correlation.

for Γ (with much smaller reduced χ^2 , compared with Figure 10(c)). Noteworthily, the $\Gamma = 10^{3.33} L_{\text{iso}}^{0.46} E_p^{-0.43}$ correlation obtained from the statistical fitting actually is consistent with our $\Gamma \propto E_{\text{iso}}^{1/8} E_p^{1/2}/(T_{90})^{1/4}$ correlation derived from the photosphere emission model. Because along with $E_p \propto (E_{\text{iso}})^{1/4}$ (or $E_p \propto (L_{\text{iso}})^{1/4}$, see Figure 1 and Figure 6), they can be transferred to each other, as shown in the following.

$$\begin{aligned}
 \Gamma &\propto E_{\text{iso}}^{1/8} E_p^{1/2}/(T_{90})^{1/4} \\
 &\propto (E_{\text{iso}}/T_{90})^{1/8} \cdot E_p^{1/2}/(T_{90})^{1/8}, \text{ with } E_p \propto (L_{\text{iso}})^{1/4} \\
 &\propto (L_{\text{iso}})^{1/8} \cdot (L_{\text{iso}}^{0.23} \cdot E_p^{-0.43})/(T_{90})^{1/8} \\
 &\propto L_{\text{iso}}^{0.36} \cdot E_p^{-0.43}/(T_{90})^{1/8}, \text{ with } T_{90} \propto (L_{\text{iso}})^{-0.5} \\
 &\propto L_{\text{iso}}^{0.36} \cdot E_p^{-0.43}/(L_{\text{iso}}^{-0.5})^{1/8} \\
 &\propto L_{\text{iso}}^{0.43} \cdot E_p^{-0.43}.
 \end{aligned} \tag{16}$$

Here, the adopted $T_{90} \propto (L_{\text{iso}})^{-0.5}$ correlation is found from Figure 12(c) for the high-efficiency sub-sample ($\epsilon_\gamma \gtrsim 80\%$).

In Figure 12(b), we compare the Γ obtained from $\Gamma = 10^{3.33} L_{\text{iso}}^{0.46} E_p^{-0.43}$ and the Γ obtained from $\Gamma \propto E_{\text{iso}}^{1/8} E_p^{1/2}/(T_{90})^{1/4}$ for the $\epsilon_\gamma \gtrsim 50\%$ sub-sample (17 bursts), the $\epsilon_\gamma \lesssim 50\%$ sub-sample (18 bursts) and the high-efficiency sub-sample ($\epsilon_\gamma \gtrsim 80\%$). Obviously, these two estimations are well centered around the equal-value line and have a linear correlation. Furthermore, for the high-efficiency sub-sample, which have the tightest $E_p \propto (E_{\text{iso}})^{1/4}$ correlation (with very small dispersion, see Figure 1), these two estimations are almost the same. For the $\epsilon_\gamma \gtrsim 50\%$ sub-sample, which have larger dispersion for the $E_p \propto (E_{\text{iso}})^{1/4}$ correlation, the above two estimations show larger dispersion, also. And for the $\epsilon_\gamma \lesssim 50\%$ sub-sample, which have the largest dispersion for the $E_p \propto (E_{\text{iso}})^{1/4}$ correlation, the above two estimations do show the largest dispersion.

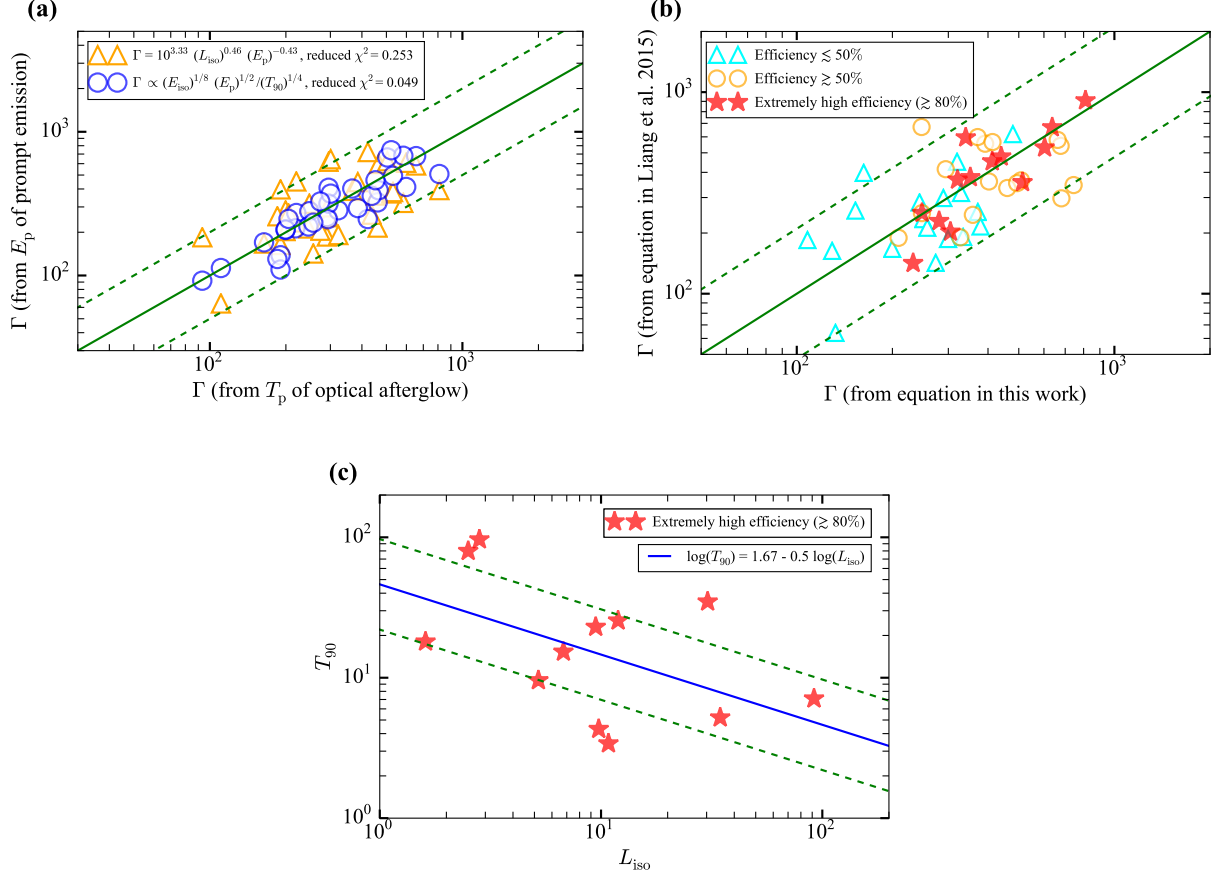


FIG. 12.— Comparison of the Γ obtained from $\Gamma \propto E_{\text{iso}}^{1/8} E_p^{1/2} / (T_{90})^{1/4}$ and $\Gamma = 10^{3.33} L_{\text{iso}}^{0.46} E_p^{-0.43}$. (a) The comparison of the Γ obtained from the optical afterglow and the Γ obtained from the prompt emission (orange triangles for $\Gamma = 10^{3.33} L_{\text{iso}}^{0.46} E_p^{-0.43}$ and blue circles for $\Gamma \propto E_{\text{iso}}^{1/8} E_p^{1/2} / (T_{90})^{1/4}$) for the better sample (35 bursts) in Figure 10(d). The different constants are used for the $\epsilon_\gamma \gtrsim 50\%$ and $\epsilon_\gamma \lesssim 50\%$ sub-samples. (b) Comparison of the Γ obtained from $\Gamma = 10^{3.33} L_{\text{iso}}^{0.46} E_p^{-0.43}$ and $\Gamma \propto E_{\text{iso}}^{1/8} E_p^{1/2} / (T_{90})^{1/4}$ for the $\epsilon_\gamma \lesssim 50\%$ (cyan triangles), the $\epsilon_\gamma \gtrsim 50\%$ (orange circles) and the high-efficiency ($\epsilon_\gamma \gtrsim 80\%$, red stars) sub-samples. Obviously, these two estimations are consistent with each other, since they can be transferred with $E_p \propto (E_{\text{iso}})^{1/4}$. (c) The $T_{90} \propto (L_{\text{iso}})^{-0.5}$ correlation, found for the high-efficiency sub-sample ($\epsilon_\gamma \gtrsim 80\%$).

3.4. The Distribution of the E_{iso}/E_k for the Whole Sample

In Figure 13, we show the distribution of the E_{iso}/E_k (indicating the efficiency ϵ_γ) for the whole sample (117 bursts). The average value is around $\sim 10^{-0.2}$ to $10^{-0.3}$, thus indicating the average efficiency of $\epsilon_\gamma \sim 33\%$ to 40% . From Figure 13, we also find that the distribution seems to consist of three Gaussian distributions. The high-efficiency peak ($\sim 10^{0.6}$) is almost consistent with the $\eta \propto 10^{0.35} \cdot E_p$ and $\Gamma \propto 10^{-0.3} \cdot E_p$ correlations (namely $E_{\text{iso}}/E_k = \eta/\Gamma \sim 10^{0.65}$) in Figure 11(a). Theoretically, for the $\epsilon_\gamma > 50\%$ case, from Equation (13) and $\eta \propto (L_{\text{iso}})^{1/4}$ we should also have $\Gamma \propto (L_{\text{iso}}/\eta)^{1/3} \propto (L_{\text{iso}}/L_{\text{iso}}^{1/4})^{1/3} \propto (L_{\text{iso}})^{1/4}$. So, the high-efficiency peak is predicted to exist. For the $\epsilon_\gamma < 50\%$ case, $E_{\text{iso}}/E_k = (R_{\text{ph}}/R_s)^{-2/3} \propto (L_{\text{iso}}/\Gamma^4)^{-2/3}$. Thus, the low-efficiency peak ($\sim 10^{-0.7}$) is the natural result of $\Gamma \propto (L_{\text{iso}})^{1/4}$, here $\Gamma = \eta$.

4. EVIDENCES IN THE SHORT GRBS WITH $\epsilon_\gamma \gtrsim 50\%$ AND

$\epsilon_\gamma \lesssim 50\%$.

For the short GRBs, similar to the long GRBs we use the judgement of $E_{\text{iso},52} = E_{k,52} = 3.7 * L_{X,45}$ ($\epsilon_\gamma = 50\%$) to get the $\epsilon_\gamma \gtrsim 50\%$ sample (4 bursts) and the $\epsilon_\gamma \lesssim 50\%$ sample (8 bursts) (see Table 8). In Figure 14(a), we show the E_p and E_{iso} distributions for these two distinguished samples. Obviously, the $\epsilon_\gamma \gtrsim 50\%$ sample and the up-most distribution for the large sample of short GRBs (Zhang et al. 2018b) (without $L_{X,45}$ detection for most) do follow the $E_p \propto (E_{\text{iso}})^{1/4}$ correlation, well consistent with the prediction of the photosphere emission model. Noteworthily, the distribution for GRB 170817A is well in the above line ($\log(E_p) = 3.24 + 0.25 \log(E_{\text{iso}})$), too. For the $\epsilon_\gamma \lesssim 50\%$ sample, as predicted the distribution is below this line (since E_p and E_{iso} are smaller). Similar to Figure 8(a) (to test whether the E_p and E_{iso} are both smaller by a factor of $E_{\text{iso}}/E_k = (R_{\text{ph}}/R_s)^{-2/3}$), in Figure 14(b) we show the distribution of E_{ratio} ($E_{\text{ratio}} = [(E_p/2.7k)^4 * (4\pi r_1^2 ac)/E_{\text{iso}}]^{1/3}$) and E_{iso}/E_k for this $\epsilon_\gamma \lesssim 50\%$ sample. Note that we exclude 3 bursts with $E_{\text{iso}} \leq 10^{50}$ ergs and we have $r_1 = 3.4 \times 10^7$

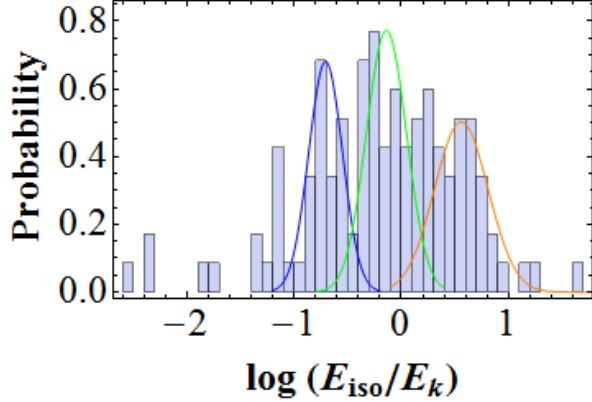


FIG. 13.— The distribution of the E_{iso}/E_k for our whole sample (117 bursts, after GRB 110213A). The mean value is around $\sim 10^{-0.2}$ to $10^{-0.3}$, thus indicating the average efficiency of $\epsilon_\gamma \sim 33\%$ to 40%. Also, the distribution seems to consist of three Gaussian distributions.

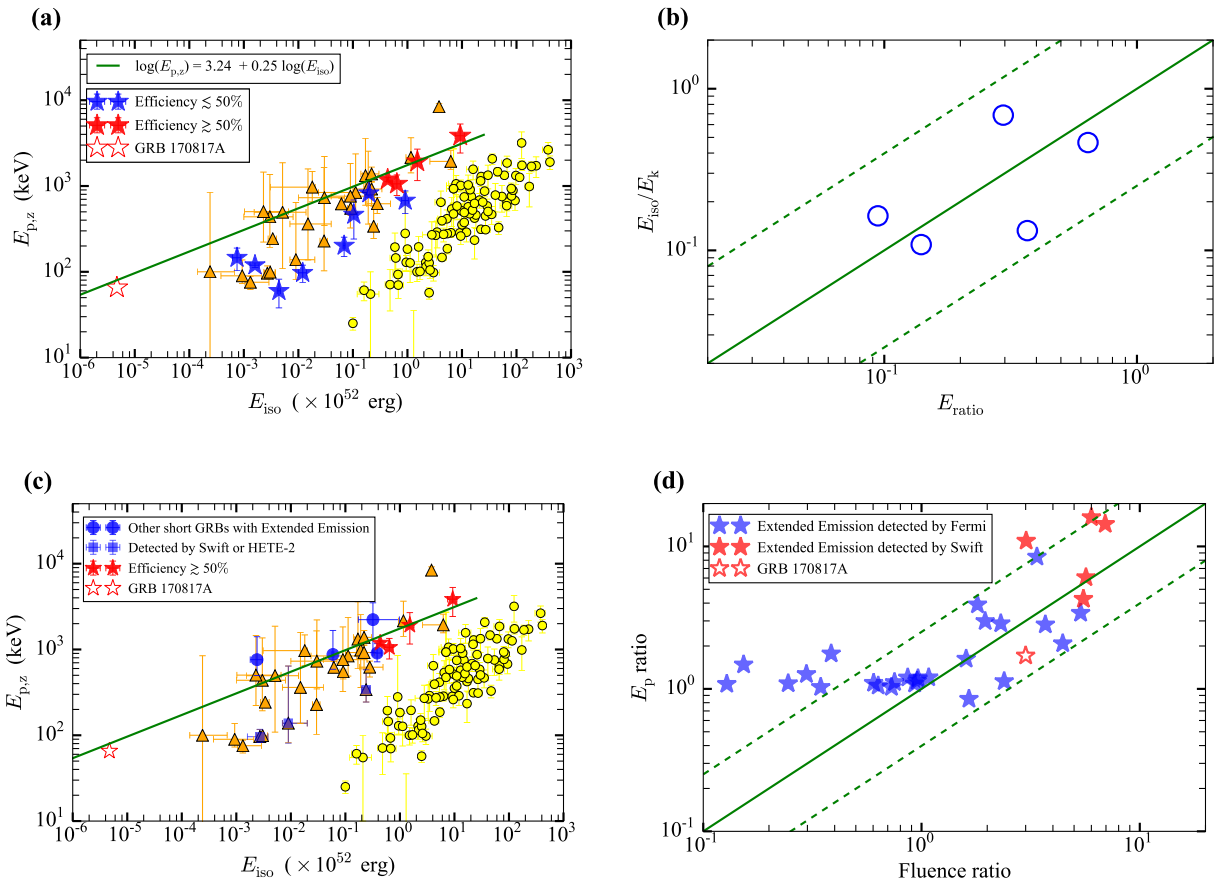


FIG. 14.— Evidences in the short GRBs. (a) The different distributions of E_p and E_{iso} for the two distinguished samples: $\epsilon_\gamma \gtrsim 50\%$ (red stars) and $\epsilon_\gamma \lesssim 50\%$ (blue stars). (b) The distribution of E_{ratio} and E_{iso}/E_k for the $\epsilon_\gamma \lesssim 50\%$ sample. (c) The E_p and E_{iso} distribution of the main pulse for other 7 bursts (blue circles and boxes), which have extended emission (see Minaev & Pozanenko 2020) and lack efficiency. Note that all the 5 bursts of the $\epsilon_\gamma \gtrsim 50\%$ sample (red stars) have extended emission, including GRB 170817A. (d) The comparison of the ratios of the E_p and the fluence (or E_{iso}) for the main pulse and the extended emission of a large extended emission sample, including the bursts without redshift (blue stars).

cm here. Still as predicted, they are found to be almost centered around the equal-value line, and have the linear correlation.

Interestingly, we find that all the bursts of the $\epsilon_\gamma \gtrsim 50\%$ sample (5 bursts, including GRB 170817A) have extended emission, and the E_p and E_{iso} distribution in Figure 14(a) is for their main pulse. To further test this finding, in Figure 14(c) we show the E_p and E_{iso} distribution of the main pulse for other 7 bursts which have extended emission (Minaev & Pozanenko 2020). It is found that, except for 3 bursts only detected by *Swift* or HETE-2 (lacking the detections in the high-energy band), other 4 bursts do follow the $\log(E_p) = 3.24 + 0.25 \log(E_{\text{iso}})$ correlation of the $\epsilon_\gamma \gtrsim 50\%$ sample, supporting the above finding again. The true E_p values for these 3 outliers are likely to be much larger. According to the above, the main pulse for the short GRBs with extended emission is likely to be produced by the photosphere emission in the unsaturated acceleration regime. Then, considering the smaller values of both the E_p and E_{iso} for their extended emission, we think that the extended emission may be produced by the transition from the unsaturated acceleration to the saturated acceleration (the E_p and E_{iso} are both smaller by the same factor of $E_{\text{iso}}/E_k = (R_{\text{ph}}/R_s)^{-2/3}$). To test this hypothesis, in Figure 14(d) we show the comparison of the ratios of the E_p and the fluence of the main pulse and the extended emission for a large extended emission sample (including the Swift/BAT bursts with redshift, Gompertz et al. 2020; and the *Fermi*/GBM bursts without redshift, Lan et al. 2020). As predicted, these two ratios are found to be almost centered around the equal-value line and have a linear correlation.

5. SUMMARY

In this work, by obtaining the prompt emission efficiency of the large GRB sample with redshift, we divide the GRB sample into three sub-samples ($\epsilon_\gamma \gtrsim 80\%$, $\epsilon_\gamma \gtrsim 50\%$ and $\epsilon_\gamma \lesssim 50\%$). Then, the well-known Amati relation (Amati et al. 2002) is well explained by the photosphere emission model. Furthermore, for each sub-sample, the characteristics of the X-ray afterglow and optical afterglow are well consistent with the prediction of the photosphere emission model. In total, large amounts of convincing observational evidences for the photosphere emission model are revealed, for the first time.

ACKNOWLEDGEMENTS

I thank Bin-Bin Zhang and Liang Li for helpful discussions. Y.-Z.M. is supported by the National Postdoctoral Program for Innovative Talents (grant no. BX20200164). I also acknowledge the use of public data from the Fermi Science Support Center, the Swift and the Konus-Wind.

APPENDIX A: THE PROBABILITY PHOTOSPHERE MODEL AND THE DISSIPATIVE PHOTOSPHERE MODEL

A1: THE PROBABILITY PHOTOSPHERE MODEL

For the traditional photosphere model, the photosphere emission is all emitted at the photospheric radius R_{ph} , where the optical depth for a photon propagating towards the observer is equal to unity ($\tau = 1$). But, if only there is an electron at any position, the photon should have a probability to be scattered there. For an expanding fireball, the photons can be last scattered at

any place in the fireball with a certain probability. Thus, the traditional spherical shell photosphere is changed to a probability photosphere, namely the probability photosphere model (Pe'er 2008). Based on careful theoretical derivation, the probability function $P(r, \Omega)$, donating the probability for a photon to be last scattered at the radius r and angular coordinate Ω , can be given as (Pe'er 2008; Beloborodov 2011; Lundman et al. 2013)

$$P(r, \Omega) = (1 + \beta) D^2 \times \frac{R_{\text{ph}}}{r^2} \exp\left(-\frac{R_{\text{ph}}}{r}\right), \quad (17)$$

where β is the jet velocity and $D = [\Gamma(1 - \beta \cdot \cos \theta)]^{-1}$ is the Doppler factor.

For the probability photosphere model, the observed photosphere spectrum is the overlapping of a series of blackbodies with different temperatures, thus its low-energy spectrum is broadened. After considering the jet with angular structure (e.g., Dai & Gou 2001; Rossi et al. 2002; Zhang & Mészáros 2002), the observed typical low-energy photon index $\alpha \sim -1.0$ (Kaneko et al. 2006; Zhang et al. 2011), spectral evolution and E_p evolutions (hard-to-soft evolution or E_p -intensity tracking, Liang & Kargatis 1996; Lu et al. 2010, 2012) can be reproduced (Lundman et al. 2013; Meng et al. 2019, 2022).

A2: THE DISSIPATIVE PHOTOSPHERE MODEL

The dissipative photosphere model (or the sub-photosphere model) considers that there is an extra energy dissipation process in the area of moderate optical depth ($1 < \tau < 10$, the sub-photosphere). Different dissipative mechanisms have been proposed, such as shocks (Rees & Mészáros 2005), magnetic reconnection (Gianios & Spruit 2007) and proton–neutron nuclear collisions (Vurm & Beloborodov 2016; Beloborodov 2017). Then, relativistic electrons (with a higher temperature than that of the photons) are generated that upscatter the thermal photons to obtain the non-thermal (broadened) high-energy spectrum.

APPENDIX B: SOME THEORETICAL DESCRIPTIONS FOR THE AFTERGLOW

B1: THE REMAINING KINETIC ENERGY IN THE AFTERGLOW PHASE (E_k) AND THE ISOTROPIC X-RAY AFTERGLOW LUMINOSITY AT 11 HOURS ($L_{X,11h}$).

In the context of the standard afterglow model (Paczynski & Rhoads 1993; Mészáros & Rees 1997), since at a late afterglow epoch (11 hours) the X-ray band is above the cooling frequency ν_c , the late-time X-ray afterglow luminosity ($L_{X,11h}$) only sensitively depends on E_k and ϵ_e (the electron equipartition parameter). Furthermore, the fraction of energy in the electrons (ϵ_e) is quite centered around 0.1, based on the large-sample afterglow analysis. Thus, E_k can be well estimated by the $L_{X,11h}$ as following (Lloyd-Ronning & Zhang 2004):

$$\begin{aligned} E_k &= 10^{52} \text{ ergs R} \left[\frac{L_{X,10h}}{10^{46} \text{ ergs s}^{-1}} \right]^{4/(2+p)} \left(\frac{1+z}{2} \right)^{-1} \\ &\quad \times \epsilon_{e,-1}^{4(1-p)/(2+p)} \epsilon_{B,-2}^{(2-p)/(2+p)} t_{10h}^{(3p-2)/(2+p)} \nu_{18}^{2(p-2)/(2+p)} \\ &\simeq 10^{52} \text{ ergs R} \left[\frac{1.1 L_{X,11h}}{10^{46} \text{ ergs s}^{-1}} \right] \left(\frac{1+z}{2} \right)^{-1} \\ &\quad \times (\epsilon_{e,-1})^{-1}, \quad (p \simeq 2) \end{aligned} \quad (18)$$

where $R = [t(10 \text{ h})/t(\text{prompt})]^{(17/16)\epsilon_e} \sim 2.27$ is the radiative losses during the first 10 hour after the prompt phase. Note that the derived E_k is 9.2 times larger in Fan & Piran (2006), since the ν_m (characteristic frequency corresponding to the minimum electron Lorentz factor) is about one and half orders smaller. Previously, it is hard to judge which constant is better. Here, using the method ($\epsilon_\gamma = 50\%$ and maximum Γ , see Section 3.1) in this work, our result ($E_{k,52} \simeq 3.7 * L_{X,45}$) is quite consistent with $E_{k,52} \simeq 2.5 * L_{X,45}$ (Fan & Piran 2006, without the inverse Compton effect).

The isotropic X-ray afterglow luminosity (in the 2-10 keV rest-frame common energy band) at 11 hours (rest frame), $L_{X,11h}$, is computed from the observed integral 0.3-10 keV unabsorbed fluxes at 11 hours ($F_{X,11h}$, estimated from the *Swift*/XRT light curve) and the measured spectral index Γ_1 (from the XRT spectrum), along with the luminosity distance D_L . The equation is as following (D'Avanzo et al. 2012):

$$L_{X,11h}(2 - 10 \text{ keV}) = 4\pi D_L^2 \cdot F_{X,11h}(0.3 - 10 \text{ keV}) \cdot \frac{\left(\frac{10}{1+z}\right)^{2-\Gamma_1} - \left(\frac{2}{1+z}\right)^{2-\Gamma_1}}{10^{2-\Gamma_1} - 0.3^{2-\Gamma_1}}. \quad (19)$$

Here, the $F_{X,11h}$ is obtained by interpolating (or extrapolating) the best-fit power law, for the XRT light curve within a selected time range including (or close to) 11 hours, to the 11 hours.

B2: THE POWER-LAW SHAPE OF THE X-RAY AFTERGLOW PREDICTED BY THE CLASSICAL HOT FIREBALL.

The “generic” afterglow model (relativistic blast-wave theory) for GRB predicts a power-law decaying multi-wavelength afterglow (Paczynski & Rhoads 1993; Mészáros & Rees 1997), due to the self-similar nature of the blastwave solution. The observed specific flux is

$$f_\nu \propto E_k^{(p+2)/4} \epsilon_e^{p-1} \epsilon_B^{(p-2)/4} t_{\text{obs}}^{-(3p-2)/4} \nu^{-p/2} \simeq \frac{(\epsilon_e E_k)}{t_{\text{obs}}} \nu^{-1}, (p \simeq 2). \quad (20)$$

REFERENCES

Abdo, A. A., Ackermann, M., Ajello, M., et al. 2009, ApJ, 706, L138
 Abramowicz, M. A., Novikov, I. D., & Paczynski, B. 1991, ApJ, 369, 175
 Acuner, Z., & Ryde, F. 2018, MNRAS, 475, 1708
 Acuner, Z., Ryde, F., Pe'er, A., et al. 2020, ApJ, 893, 128
 Amati, L., Frontera, F., Tavani, M., et al. 2002, A&A, 390, 81
 Axelsson, M., Baldini, L., Barbiellini, G., et al. 2012, ApJ, 757, L31
 Axelsson, M., & Borgonovo, L. 2015, MNRAS, 447, 3150
 Band, D., Matteson, J., Ford, L., et al. 1993, ApJ, 413, 281
 Bégué, D., & Pe'er, A. 2015, ApJ, 802, 134
 Beloborodov, A. M. 2011, ApJ, 737, 68
 Beloborodov, A. M. 2017, ApJ, 838, 125
 Burgess, J. M., Greiner, J., Bégué, D., & Berlato, F. 2017, arXiv:1710.08362
 Burgess, J. M., Bégué, D., Greiner, J., et al. 2020, Nature Astronomy, 4, 174
 Dai, Z. G., & Gou, L. J. 2001, ApJ, 552, 72
 D'Avanzo, P., Salvaterra, R., Sbarufatti, B., et al. 2012, MNRAS, 425, 506
 Deng, W., & Zhang, B. 2014, ApJ, 785, 112
 Dereli-Bégué, H., Pe'er, A., & Ryde, F. 2020, ApJ, 897, 145
 Fan, Y., & Piran, T. 2006, MNRAS, 369, 197
 Fan, Y.-Z., Wei, D.-M., Zhang, F.-W., & Zhang, B.-B. 2012, ApJ, 755, L6
 Gao, H., Wang, X.-G., Mészáros, P., et al. 2015, ApJ, 810, 160
 Geng, J.-J., Huang, Y.-F., Wu, X.-F., Zhang, B., & Zong, H.-S. 2018, ApJS, 234, 3
 Geng, J.-J., Zhang, B., Kölligan, A., Kuiper, R., & Huang, Y.-F. 2019, ApJ, 877, L40
 Ghirlanda, G., Pescalli, A., & Ghisellini, G. 2013, MNRAS, 432, 3237
 Ghirlanda, G., Nappo, F., Ghisellini, G., et al. 2018, A&A, 609, A112
 Ghisellini, G., Ghirlanda, G., Nava, L., et al. 2010, MNRAS, 403, 926
 Giannios, D., & Spruit, H. C. 2007, A&A, 469, 1
 Goldstein, A., Burgess, J. M., Preece, R. D., et al. 2012, ApJS, 199, 19
 Gompertz, B. P., Levan, A. J., & Tanvir, N. R. 2020, ApJ, 895, 58
 Goodman, J. 1986, ApJ, 308, L47
 Gruber, D., Goldstein, A., Weller von Ahlefeld, V., et al. 2014, ApJS, 211, 12

This power-law behavior ($f \sim t_{\text{obs}}^{-1}$) is well consistent with the observations of the optical and radio afterglows. But several surprising emission components (the steep decay $f \sim t_{\text{obs}}^{-3}$ phase, the plateau $f \sim t_{\text{obs}}^{-0.5}$ phase, and the flare) in the early X-ray afterglow are revealed by the *Swift* observations (Zhang et al. 2006), which are not predicted by the above standard (hot fireball) model. These extra components imply that an extra energy injection (internal or external) may exist, which can be magnetic-dominated.

B3: THE REVERSE SHOCK IN THE OPTICAL AFTERGLOW PREDICTED BY THE CLASSICAL HOT FIREBALL.

For the classical hot fireball (the magnetic field in the ejecta is dynamically unimportant, namely the magnetization parameter $\sigma \equiv B'^2/(4\pi n'_p m_p c^2) \ll 1$), a strong reverse shock (propagating back across the GRB ejecta to decelerate it) is predicted in the early optical afterglow phase (Mészáros & Rees 1997; Sari & Piran 1999). This prediction is almost confirmed by the discovery of a very bright optical flash in GRB 990123 while gamma-ray burst is still active. Later on, much more reverse shock signals are found. The light curve of the reverse shock declines more rapidly ($f \sim t^{-2}$) than the forward shock ($f \sim t^{-1}$), and rises more rapidly ($f \gtrsim t^3$) than the forward shock ($f \sim t^2$) before the peak time.

B4: THE FERMI/LAT (GEV EMISSION) LIGHT CURVE FROM RADIATIVE FIREBALL.

For the generic afterglow model, the total energy of the fireball remains constant (the adiabatic case) after the forward shock starts to decelerate (entering the self-similar phase). However, there could be another case that the total energy of the fireball decreases (the radiative case), since a large fraction of the dissipated energy is radiated away (by magnetic reconnection or electron-proton collisions) (Ghisellini et al. 2010). For this radiative fireball, the light curve (after the peak time) declines more rapidly ($f \sim t^{-10/7}$), $\Gamma \propto t^{-3/7}$ ($\Gamma \propto t^{-3/8}$ for adiabatic case), and the peak time is much earlier ($t_{\text{peak}} = 0.44t_{\text{dec}}$, $t_{\text{peak}} = 0.63t_{\text{dec}}$ for adiabatic case; t_{dec} is the deceleration time).

Guiriec, S., Connaughton, V., Briggs, M. S., et al. 2011, *ApJ*, 727, L33

Guiriec, S., Daigne, F., Hascoët, R., et al. 2013, *ApJ*, 770, 32

Hou, S.-J., Zhang, B.-B., Meng, Y.-Z., et al. 2018, *ApJ*, 866, 13

Kaneko, Y., Preece, R. D., Briggs, M. S., et al. 2006, *ApJS*, 166, 298

Kobayashi, S., Piran, T., & Sari, R. 1997, *ApJ*, 490, 92

Lan, L., Lu, R.-J., Lü, H.-J., et al. 2020, *MNRAS*, 492, 3622

Larsson, J., Racusin, J. L., & Burgess, J. M. 2015, *ApJ*, 800, L34

Lazzati, D., Morsony, B. J., Margutti, R., & Begelman, M. C. 2013, *ApJ*, 765, 103

Li, L., Liang, E.-W., Tang, Q.-W., et al. 2012, *ApJ*, 758, 27

Li, L., Wang, Y., Shao, L., et al. 2018, *ApJS*, 234, 26

Li, L. 2019a, *ApJS*, 242, 16

Li, L., Geng, J.-J., Meng, Y.-Z., et al. 2019b, *ApJ*, 884, 109

Li, L. 2019c, *ApJS*, 245, 7

Li, L. 2020, *ApJ*, 894, 100

Li, L., Ryde, F., Pe'er, A., et al. 2021, *ApJS*, 254, 35

Liang, E., & Kargatis, V. 1996, *Nature*, 381, 49

Liang, E.-W., Li, L., Gao, H., et al. 2013, *ApJ*, 774, 13

Liang, E.-W., Lin, T.-T., Lü, J., et al. 2015, *ApJ*, 813, 116

Lin, D.-B., Liu, T., Lin, J., et al. 2018, *ApJ*, 856, 90

Lloyd-Ronning, N. M., & Zhang, B. 2004, *ApJ*, 613, 477

Lu, R.-J., Hou, S.-J., & Liang, E.-W. 2010, *ApJ*, 720, 1146

Lu, R.-J., Wei, J.-J., Liang, E.-W., et al. 2012, *ApJ*, 756, 112

Lundman, C., Pe'er, A., & Ryde, F. 2013, *MNRAS*, 428, 2430

Lü, J., Zou, Y.-C., Lei, W.-H., et al. 2012, *ApJ*, 751, 49

Meng, Y.-Z., Geng, J.-J., Zhang, B.-B., et al. 2018, *ApJ*, 860, 72

Meng, Y.-Z., Liu, L.-D., Wei, J.-J., Wu, X.-F., & Zhang, B.-B. 2019, *ApJ*, 882, 26

Meng, Y.-Z., Geng, J.-J., & Wu, X.-F. 2022, *MNRAS*, 509, 6047

Mészáros, P. & Rees, M. J. 1997, *ApJ*, 476, 232

Mészáros, P., & Rees, M. J. 2000, *ApJ*, 530, 292

Mészáros, P. 2002, *ARA&A*, 40, 137

Minaev, P. Y. & Pozanenko, A. S. 2020, *MNRAS*, 492, 1919

Nava, L., Salvaterra, R., Ghirlanda, G., et al. 2012, *MNRAS*, 421, 1256

Paczynski, B. 1986, *ApJ*, 308, L43

Paczynski, B. & Rhoads, J. E. 1993, *ApJ*, 418, L5

Parsonat, T. & Lazzati, D. 2022, *ApJ*, 926, 104

Pe'er, A. 2008, *ApJ*, 682, 463

Pe'er, A., & Ryde, F. 2011, *ApJ*, 732, 49

Pe'er, A., Barlow, H., O'Mahony, S., et al. 2015, *ApJ*, 813, 127

Piran, T. 1999, *Phys. Rep.*, 314, 575

Rees, M. J., & Meszaros, P. 1994, *ApJ*, 430, L93

Rees, M. J., & Mészáros, P. 2005, *ApJ*, 628, 847

Rossi, E., Lazzati, D., & Rees, M. J. 2002, *MNRAS*, 332, 945

Ruffini, R., Siutsou, I. A., & Vereshchagin, G. V. 2013, *ApJ*, 772, 11

Ryde, F. 2004, *ApJ*, 614, 827

Ryde, F. 2005, *ApJ*, 625, L95

Ryde, F., & Pe'er, A. 2009, *ApJ*, 702, 1211

Ryde, F., Axelsson, M., Zhang, B. B., et al. 2010, *ApJ*, 709, L172

Ryde, F., Lundman, C., & Acuner, Z. 2017, *MNRAS*, 472, 1897

Sari, R. & Piran, T. 1999, *ApJ*, 520, 641

Song, X. & Meng, Y.-Z. 2022, arXiv:2203.00882

Thompson, C. 1994, *MNRAS*, 270, 480

Tsvetkova, A., Frederiks, D., Golenetskii, S., et al. 2017, *ApJ*, 850, 161

Uhm, Z. L. & Zhang, B. 2014, *Nature Physics*, 10, 351

Vereshchagin, G. V. & Siutsou, I. A. 2020, *MNRAS*, 494, 1463

von Kienlin, A., Meegan, C. A., Paciesas, W. S., et al. 2020, *ApJ*, 893, 46

Vurm, I., & Beloborodov, A. M. 2016, *ApJ*, 831, 175

Vyas, M. K., Pe'er, A., & Eichler, D. 2021, *ApJ*, 908, 9

Wang, K., Lin, D.-B., Wang, Y., et al. 2020, *ApJ*, 899, 111

Wygoda, N., Guetta, D., Mandich, M. A., & Waxman, E. 2016, *ApJ*, 824, 127

Xue, L., Zhang, F.-W., & Zhu, S.-Y. 2019, *ApJ*, 876, 77

Yang, J., Chand, V., Zhang, B.-B., et al. 2020, *ApJ*, 899, 106

Yi, S.-X., Wu, X.-F., Zou, Y.-C., et al. 2020, *ApJ*, 895, 94

Yu, H.-F., van Eerten, H. J., Greiner, J., et al. 2015, *A&A*, 583, A129

Yu, H.-F., Preece, R. D., Greiner, J., et al. 2016, *A&A*, 588, A135

Zhang, B., & Mészáros, P. 2002a, *ApJ*, 571, 876

Zhang, B., Fan, Y. Z., Dyks, J., et al. 2006, *ApJ*, 642, 354

Zhang, B., Liang, E., Page, K. L., et al. 2007, *ApJ*, 655, 989

Zhang, B. 2011, *Comptes Rendus Physique*, 12, 206

Zhang, B., & Yan, H. 2011, *ApJ*, 726, 90

Zhang, B. 2020, *Nature Astronomy*, 4, 210

Zhang, B.-B., Zhang, B., Liang, E.-W., et al. 2011, *ApJ*, 730, 141

Zhang, B.-B., Zhang, B., Castro-Tirado, A. J., et al. 2018a, *Nature Astronomy*, 2, 69

Zhang, B.-B., Zhang, B., Sun, H., et al. 2018b, *Nature Communications*, 9, 447

Zhang, B.-B., Liu, Z.-K., Peng, Z.-K., et al. 2021, *Nature Astronomy*, 5, 91

Zhang, Z. J., Zhang, B.-B., & Meng, Y.-Z. 2021, arXiv:2109.14252

TABLE 2

FITTING RESULTS OF THE TIME-INTEGRATED SPECTRUM FOR THE BURSTS WITH EXTREMELY HIGH EFFICIENCY (DETECTED BY *Fermi*)

GRB	α (CPL)	E_c (CPL)	F (CPL)	α (Band)	β (Band)	E_p (Band)	F (Band)	ΔDIC (Band-CPL)	p_{DIC} (CPL)	p_{DIC} (Band)
110818A	-1.18 ^{+0.15} _{-0.15}	352 ⁺¹⁶⁹ ₋₁₆₁	0.18 ^{+0.12} _{-0.06} $\times 10^{-6}$	0.48 ^{+0.50} _{-0.56}	-1.70 ^{+0.07} _{-0.07}	42 ⁺⁷ ₋₇	0.46 ^{+1.54} _{-0.35} $\times 10^{-6}$	-141.4	-2.9	-151.3
120729A	-0.55 ^{+0.04} _{-0.04}	163 ⁺²³ ₋₂₄	0.17 ^{+0.05} _{-0.04} $\times 10^{-6}$	-0.55 ^{+0.04} _{-0.04}	-4.93 ^{+2.44} _{-2.66}	229 ⁺³⁰ ₋₂₉	0.19 ^{+0.07} _{-0.04} $\times 10^{-6}$	-1.3	1.9	1.4
131108A	-0.93 ^{+0.02} _{-0.02}	380 ⁺²⁵ ₋₂₆	1.36 ^{+0.12} _{-0.10} $\times 10^{-6}$	0.66 ^{+0.08} _{-0.08}	-1.60 ^{+0.01} _{-0.01}	61 ⁺⁰ ₋₀	3.54 ^{+0.69} _{-0.61} $\times 10^{-6}$	599.9	2.9	1.7
150821A	-1.19 ^{+0.02} _{-0.02}	419 ⁺³⁵ ₋₃₅	0.64 ^{+0.05} _{-0.05} $\times 10^{-6}$	-1.18 ^{+0.03} _{-0.03}	-3.87 ^{+1.71} _{-3.16}	313 ⁺³¹ ₋₃₂	0.76 ^{+0.19} _{-0.15} $\times 10^{-6}$	-8.0	2.9	-1.5
161014A	-0.74 ^{+0.10} _{-0.10}	144 ⁺²⁴ ₋₂₄	0.22 ^{+0.07} _{-0.05} $\times 10^{-6}$	1.52 ^{+0.34} _{-0.34}	-1.74 ^{+0.04} _{-0.04}	48 ⁺² ₋₂	0.63 ^{+0.82} _{-0.37} $\times 10^{-6}$	3.0	1.6	-40.0
170214A	-1.06 ^{+0.01} _{-0.01}	570 ⁺²⁶ ₋₂₆	1.53 ^{+0.08} _{-0.06} $\times 10^{-6}$	-1.05 ^{+0.01} _{-0.01}	-2.77 ^{+0.36} _{-0.12}	510 ⁺²² ₋₂₂	1.81 ^{+0.15} _{-0.14} $\times 10^{-6}$	-10.6	3.0	2.7

Note—For 120729A, 150821A and 170214A, the high-energy spectral indices for BAND function are very small (-4.93, -3.87 and -2.77), while the low-energy spectral indices and peak energy for BAND function and COM model are very similar. For 110818A, 131108A and 161014A, the low-energy spectral indices for BAND function are extremely hard (0.48, 0.66, 1.52), and the peak energy is extremely small (42, 61, 48). Thus, the COM model is surely the best-fit model.

TABLE 3

THE BURSTS WITH ALMOST SAME E_{ratio} AND $E_{\text{iso}}/E_{\text{k}}$ AND THEIR POWER-LAW SLOPE OF THE X-RAY AFTERGLOW LIGHT CURVE.

Bursts after GRB 110213A				Bursts before GRB 110213A			
GRB	$E_{\text{iso}}/[\frac{3.7*L_{X,11}}{(1+z)/2}]$	E_{ratio}	X-ray slope	GRB	$E_{\text{iso}}/[\frac{3.7*L_{X,11}}{(1+z)/2}]$	E_{ratio}	X-ray slope
130420A	0.653	0.644 ^a	-0.900	050922C	0.898	0.821	-1.200
130831A	0.157	0.156	-0.959	060210	0.751	0.597	-0.970
131117A	0.491	0.546	-0.998	060306	0.567	0.435	-1.047
140213A	0.197	0.218	-1.070	080603B	0.629	0.528	-0.850
150301B	1.190	1.16	-1.179	091018	0.112	0.092	-1.160
150403A	1.100	1.21	-1.140	091020	0.912	0.831	-1.090
170705A	0.289	0.307	-0.969	100621A	0.159	0.193	-0.987

^a $E_{\text{iso}}/E_{\text{k}} = (R_{\text{ph}}/R_s)^{-2/3}$

TABLE 4
THE OBSERVED QUANTITIES AND INFERRED EFFICIENCY FOR THE $\epsilon_\gamma \lesssim 50\%$ SUB-SAMPLE AFTER GRB 110213A.

$\epsilon_\gamma \lesssim 50\%$ sub-sample (62 bursts)									
GRB	z	$E_{p,z}$ (keV)	E_{iso} (10^{52} erg)	$L_{\text{X,11}}$ (10^{45} erg s $^{-1}$)	$E_{\text{iso}} / [\frac{3.7 * L_{\text{X,11}}}{(1+z)^{1/2}}]$	E_{ratio}	$(R_{\text{ph}}/R_s)^{-2/3}$	Γ	$T_{90,i}$ s
110213A	1.46	183.83 ± 32.15	6.9	3.22	0.713	0.225	0.283	157	11.9
110213B	1.083	256 ± 40	7.04	3.66	0.541	0.348			
110715A	0.82	216.58 ± 12.74	4.97	9.99	0.122	0.313			
111209A	0.677	520 ± 89	5.2	2.95	0.399	0.991			
111228A	0.7156	74 ± 53	1.65	3.24	0.118	0.056			
120326A	1.798	115 ± 19	3.82	15.6	0.093	0.147			
120804A	1.3	283 ± 62	0.657	1.09	0.187	0.877			
120811C	2.671	203.98 ± 19.55	8.81	7.25	0.603	0.239			
120907A	0.97	241.16 ± 67.27	0.18	1.02	0.047	1.09			
121211A	1.023	202.76 ± 32.05	0.14	2.54	0.015	0.942			
130420A	1.297	131.59 ± 7.2	6.29	2.99	0.653	0.149	0.644	149	45.7
130612A	2.006	186 ± 32	0.719	0.32	0.913	0.487	0.653	193	1.9
130701A	1.16	192.24 ± 8.64	2.62	1.32	0.580	0.33			
130702A	0.145	17.2 ± 5.7	0.064	1.01	0.010	0.028			
130831A	0.48	81.4 ± 13.32	0.805	1.02	0.157	0.156	0.154	73	11.9
130925A	0.347	110.94 ± 3.1	15.	14.6	0.187	0.089			
131117A	4.042	222 ± 37	1.03	1.43	0.491	0.546			
131231A	0.6439	292.52 ± 6.06	21.1	13.	0.361	0.288	0.142	145	17.7
140213A	1.2076	191.24 ± 7.85	8.88	13.4	0.197	0.218			
140226A	1.98	1234 ± 235	5.68	1.71	1.340	3.05			
140304A	5.283	775.06 ± 173.37	10.3	5.19	1.690	1.34			
140506A	0.889	373.19 ± 61.49	1.4	5.88	0.060	0.986			
140508A	1.027	533.46 ± 28.44	22.5	14.4	0.428	0.629			
140512A	0.72	826 ± 201.24	7.25	6.98	0.241	2.64			
140515A	6.32	376 ± 108	5.38	3.15	1.690	0.636			
140606B	0.384	352 ± 46	0.25	1.	0.047	1.62			
140620A	2.04	230.19 ± 33.87	7.28	11.4	0.263	0.299			
140801A	1.32	$250.6 \pm 7.$	5.55	1.87	0.930	0.366			
140907A	1.21	313 ± 21	2.71	3.58	0.226	0.626			
141109A	2.993	763 ± 303	33.1	10.	1.780	0.891			
141221A	1.452	450.62 ± 87.15	2.46	1.11	0.734	1.05	0.965	202	9.7
141225A	0.915	342.71 ± 52.13	0.859	0.494	0.450	1.04			
150206A	2.09	704.52 ± 71.07	61.9	21.1	1.220	0.651			
150301B	1.5169	460.51 ± 90.95	1.99	0.567	1.190	1.16			
150323A	0.59	151.05 ± 14.31	1.26	0.427	0.632	0.306			
150403A	2.06	1311.74 ± 53.09	116.	43.9	1.100	1.21			
150514A	0.807	116.72 ± 10.19	0.878	1.26	0.171	0.245			
150727A	0.313	195.05 ± 25.18	0.2	0.062	0.575	0.794			
150818A	0.282	128 ± 37	0.1	0.09	0.193	0.571			
151027A	0.81	366.76 ± 61.78	3.3	6.17	0.131	0.724			
151029A	1.423	82 ± 17	0.288	0.232	0.407	0.221			
160227A	2.38	222 ± 55	5.56	14.6	0.174	0.311			
160509A	1.17	770.74 ± 20.82	113.	37.8	0.877	0.6			
160623A	0.37	756.24 ± 19.18	25.3	14.8	0.317	0.963			
160804A	0.736	123.93 ± 7.25	2.7	1.16	0.543	0.182			
161017A	2.013	718.83 ± 122.83	8.3	4.35	0.777	1.31			
161117A	1.549	205.62 ± 7.76	13.	7.04	0.637	0.212			
161219B	0.1475	$71. \pm 19.3$	0.012	0.778	0.002	0.533			
170113A	1.968	333.92 ± 174.49	0.924	6.	0.061	0.976			
170604A	1.329	512 ± 168	4.7	4.61	0.321	1.			
170607A	0.557	174.06 ± 14.06	0.915	3.1	0.062	0.411			
170705A	2.01	294.61 ± 23.01	18.	25.3	0.289	0.307			
170903A	0.886	180 ± 25	0.865	3.02	0.073	0.438			
171205A	0.0368	125^{+141}_{-37}	0.002	0.003	0.116	1.98			
171222A	2.409	694 ± 12	8.94	5.83	0.706	1.22			
180205A	1.409	205 ± 34	0.972	1.63	0.194	0.501			
180620B	1.1175	372 ± 105	3.04	12.4	0.070	0.758			
180720B	0.654	1052 ± 26	34.	32.	0.237	1.36			
180728A	0.117	108 ± 8	0.233	1.11	0.032	0.343			
181201A	0.45	220 ± 9	10.	11.7	0.168	0.253			
190106A	1.859	489 ± 257	9.96	14.1	0.272	0.735			
190114C	0.4245	929.3 ± 9.4	27.	9.3	0.560	1.24			

TABLE 5
THE OBSERVED QUANTITIES AND INFERRED EFFICIENCY FOR THE $\epsilon_\gamma \gtrsim 50\%$ SUB-SAMPLE AFTER GRB 110213A.

GRB	z	$\epsilon_\gamma \gtrsim 50\%$ sub-sample (40 bursts)					
		$E_{p,z}$ (keV)	E_{iso} (10^{52} erg)	$L_{\text{X,11}}$ (10^{45} erg s $^{-1}$)	$E_{\text{iso}}/[\frac{3.7 \cdot L_{\text{X,11}}}{(1+z)/2}]$	η/Γ	Γ
110422A	1.77	429.35 ± 8.31	74.700	5.450	5.140		
110503A	1.61	574.2 ± 31.32	21.300	4.390	1.710		
110731A	2.83	1223 ± 75.4	31.500	4.650	3.510	1.722	500
110918A	0.98	665.28 ± 79.2	271.000	39.100	1.850		
111008A	5.	624 ± 186	41.400	9.390	3.580		
120119A	1.728	499.91 ± 21.71	40.200	4.100	3.610		
120711A	1.405	2552 ± 91	204.000	39.800	1.660	7.587	258
120712A	4.1745	642 ± 134.5	15.200	2.310	4.600		
120909A	3.93	961.41 ± 125.42	69.000	7.570	6.070	5.060	288
121128A	2.2	244.19 ± 9.61	10.100	1.000	4.340	3.891	332
130408A	3.76	1289.96 ± 204.68	32.400	5.570	3.740		
130427A	0.34	1105.4 ± 7.3	89.000	17.000	0.947	1.050	471
130505A	2.27	1939.11 ± 85.02	438.000	29.400	6.590		
130514A	3.6	506 ± 193	49.500	5.730	5.370		
130518A	2.488	1388.34 ± 55.23	216.000	6.000	17.000		
130610A	2.092	840.81 ± 344.98	5.780	0.645	3.750	6.465	204
130907A	1.24	866.88 ± 35.84	385.000	23.900	4.870		
131030A	1.29	448.84 ± 13.74	32.700	7.060	1.430		
131105A	1.686	713.18 ± 46.18	15.300	3.340	1.660		
140206A	2.73	1780.44 ± 119.77	278.000	26.800	5.220		
140419A	3.96	1398.72 ± 188.48	228.000	10.800	14.200		
140423A	3.26	516.74 ± 64.73	43.800	4.720	5.350	6.019	303
140629A	2.275	282 ± 56	4.400	0.575	3.390		
140703A	3.14	861.25 ± 148.3	18.400	3.280	3.130		
141004A	0.573	231 ± 44	0.210	0.051	0.877		
141028A	2.33	979.59 ± 53.39	51.000	7.460	3.070		
141220A	1.3195	418.8 ± 24.17	2.290	0.322	2.230		
150314A	1.758	957.28 ± 19.06	76.800	5.090	5.620		
151021A	2.33	566.1 ± 43.29	113.000	4.470	11.400		
160131A	0.97	1282.47 ± 453.1	87.000	6.990	3.310		
160625B	1.406	1134.34 ± 15.51	510.000	39.200	4.230		
161023A	2.708	604.4 ± 137.2	68.000	5.900	5.780		
161129A	0.645	240.84 ± 70.09	0.783	0.059	2.970		
170202A	3.645	1147 ± 771	17.000	4.420	2.410		
171010A	0.3285	227.17 ± 9.3	18.000	2.880	1.123		
180325A	2.248	993.89 ± 162.4	23.000	1.300	7.770		
180329B	1.998	146 ± 28	4.690	0.995	1.910		
180914B	1.096	977 ± 61	370.000	7.600	13.800		
181020A	2.938	1461 ± 225	82.800	4.560	9.660		
181110A	1.505	120 ± 68	11.000	0.937	3.970		

TABLE 6
THE OBSERVED QUANTITIES, INFERRED EFFICIENCY (E_{ratio} AND $(R_{\text{ph}}/R_s)^{-2/3}$) AND INFERRED Γ (FROM $T_{p,\text{op}}$ AND PROMPT EMISSION) FOR THE BURSTS WITH $T_{p,\text{op}}$ DETECTION.

GRB	z	$dE_{p,z}/E_{p,z}$	$\epsilon_{\gamma} \lesssim 50\%$ sub-sample (24 bursts)									
			$E_{p,z}$ (keV)	E_{iso} (10^{52} erg)	E_{ratio}	$(R_{\text{ph}}/R_s)^{-2/3}$	$T_{90,i}$ s	$T_{p,\text{op}}$ s	Γ_{op}	Γ_E	Γ_L	
060124	2.3	0.176	635.0 ± 112.0	43.000	0.640	0.362	72.2	631.0	220.0	272.0	451.0	14.200
090618	0.54	0.059	156.0 ± 9.2	25.300	0.267	0.710	67.7	91.2	319.0	128.0	340.0	2.050
090926A	2.11	0.028	908.0 ± 25.0	200.000	0.617	0.732	4.3	8.1	851.0	798.0	828.0	74.000
091020	1.71	0.037	507.0 ± 19.0	7.910	0.833	0.689	10.8	135.0	295.0	316.0	254.0	3.300
100728B	2.11	0.116	404.0 ± 47.0	7.240	0.716	1.230	3.9	33.9	462.0	360.0	216.0	1.860
100814A	1.44	0.093	344.0 ± 32.0	8.200	0.491	0.444	60.8	589.0	164.0	170.0	167.0	0.920
110213A	1.46	0.087	241.0 ± 21.0	6.400	0.332	0.299	11.9	324.0	199.0	207.0	284.0	2.090
120922A	3.1	0.167	156.0 ± 26.0	20.000	0.234	0.261	44.5	891.0	190.0	138.0	398.0	2.900
130420A	1.3	0.054	331.0 ± 18.0	7.190	0.653	0.599	45.7	356.0	190.0	176.0	109.0	0.350
130612A	2.01	0.172	186.0 ± 32.0	0.716	0.488	0.443	1.9	110.0	246.0	219.0	212.0	0.875
130831A	0.48	0.164	80.9 ± 13.3	0.757	0.158	0.163	11.9	724.0	93.3	92.0	185.0	0.296
131231A	0.64	0.042	288.0 ± 12.0	20.000	0.288	0.299	17.7	100.0	240.0	237.0	239.0	1.700
140629A	2.28	0.199	282.0 ± 56.0	6.000	0.418	0.444	7.9	151.0	293.0	246.0	298.0	2.700
$dE_{p,z}/E_{p,z} \gtrsim 0.2$												
050922C	2.2	0.266	417.0 ± 111.0	4.530	0.773	0.739	2.	132.0	401.0	408.0	619.0	19.000
060210	3.91	0.323	575.0 ± 186.0	41.500	0.568	0.408	51.9	676.0	248.0	280.0	316.0	5.960
060418	1.49	0.250	571.0 ± 143.0	12.800	0.832	0.738	41.4	151.0	244.0	255.0	187.0	1.890
060607A	3.08	0.348	575.0 ± 200.0	10.900	0.886	0.774	25.	178.0	271.0	284.0	191.0	2.000
070110	2.35	0.460	370.0 ± 170.0	5.500	0.618	0.200	26.4	1170.0	135.0	207.0	117.0	0.451
081007	0.53	0.246	61.0 ± 15.0	0.170	0.178	1.090	6.5	123.0	152.0	77.1	85.8	0.043
091029	2.75	0.287	230.0 ± 66.0	7.400	0.297	0.317	10.5	407.0	218.0	213.0	234.0	1.320
100906A	1.73	0.348	158.0 ± 55.0	33.400	0.220	1.220	33.1	100.0	396.0	160.0	366.0	2.450
130215A	0.6	0.408	248.0 ± 101.0	2.500	0.471	0.447	90.	741.0	111.0	113.0	63.9	0.084
141109A	2.93	0.404	750.0 ± 303.0	31.000	0.891	0.150	23.5	955.0	193.0	376.0	240.0	4.200
141221A	1.45	0.228	372.0 ± 85.0	1.900	0.888	0.723	9.7	110.0	216.0	233.0	142.0	0.700
$\epsilon_{\gamma} \gtrsim 50\%$ sub-sample (23 bursts)												
GRB	z	$dE_{p,z}/E_{p,z}$	$E_{p,z}$ (keV)	E_{iso} (10^{52} erg)	E_{ratio}	η/Γ	$T_{90,i}$ s	$T_{p,\text{op}}$ s	Γ_{op}	Γ_E	Γ_L	L_{iso} (10^{52} erg s $^{-1}$)
990123	1.6	0.043	2030.0 ± 88.0	239.000	1.700	1.150	23.9	47.9	656.0	677.0	417.0	35.300
060605	3.78	0.512	490.0 ± 251.0	2.830	1.120	3.610	16.6	479.0	200.0	209.0	146.0	0.951
061121	1.31	0.093	1290.0 ± 120.0	26.100	1.940	10.300	7.7	162.0	301.0	543.0	332.0	14.100
071112C	0.82	0.546	597.0 ± 326.0	1.600	1.760	1.950	2.9	178.0	187.0	333.0	89.8	0.400
080319B	0.94	0.013	1260.0 ± 17.0	150.000	1.050	0.134	23.	17.4	810.0	508.0	281.0	9.590
080804	2.2	0.056	809.0 ± 45.0	11.500	1.370	0.443	10.6	63.1	437.0	358.0	189.0	2.690
080810	3.35	0.121	1490.0 ± 180.0	39.100	2.060	1.330	24.4	117.0	453.0	460.0	257.0	9.270
080916C	4.35	0.089	2760.0 ± 246.0	560.000	1.930	0.035	11.5	6.2	2060.0	1050.0	600.0	104.000
081203A	2.1	1.200	1540.0 ± 1854.0	35.000	2.240	3.020	96.4	309.0	274.0	327.0	146.0	2.810
090323	3.57	0.108	1900.0 ± 206.0	390.000	1.320	3.580	29.1	200.0	504.0	663.0	446.0	38.500
090812	2.45	0.449	2020.0 ± 908.0	40.300	3.060	0.496	9.5	47.9	583.0	681.0	229.0	9.550
090902B	1.82	0.015	2020.0 ± 31.0	440.000	1.380	0.094	6.9	8.5	1390.0	994.0	529.0	58.900
100414A	1.39	0.020	1490.0 ± 29.0	76.900	1.640	0.281	9.2	34.7	622.0	638.0	226.0	7.000
110731	2.83	0.057	1210.0 ± 69.0	40.000	1.550	0.041	1.75	5.0	1410.0	805.0	459.0	27.000
120711A	1.4	0.039	2340.0 ± 91.0	150.000	2.400	7.910	17.2	240.0	328.0	744.0	266.0	15.200
120909A	3.93	0.067	1820.0 ± 123.0	72.900	2.190	2.400	23.3	288.0	366.0	557.0	210.0	7.190
130427A	0.34	0.009	1380.0 ± 13.0	80.900	1.450	1.260	46.1	21.9	599.0	413.0	435.0	27.000
130610A	2.09	0.419	912.0 ± 382.0	6.810	1.920	3.150	7.	204.0	260.0	395.0	171.0	2.400
160629A	3.33	0.074	1280.0 ± 95.0	47.000	1.580	0.688	14.9	81.3	531.0	494.0	272.0	9.100
061007	1.26	0.030	902.0 ± 27.0	88.100	0.804 ^a	2.220	25.5	74.1	466.0	392.0	427.0	17.400
110205A	2.22	0.335	714.0 ± 239.0	56.000	0.685 ^a	8.540	79.8	813.0	205.0	248.0	193.0	2.500
121128A	2.2	0.050	198.0 ± 10.0	14.000	0.197 ^a	1.220	3.1	74.1	422.0	247.0	516.0	6.400
140423A	3.26	0.122	533.0 ± 65.0	56.000	0.464 ^a	1.550	22.3	200.0	385.0	294.0	319.0	5.660

^a $\epsilon_{\gamma} \gtrsim 50\%$ judged from $E_{\text{iso}}/E_{\text{k}}$.

TABLE 7
THE OBSERVED QUANTITIES AND THE PROPERTY OF $E_{\text{iso}}/L_{\text{X,11}}$ FOR THE BURSTS WITH MAXIMUM Γ .

GRB	z	$T_{90,i}$ s	$dE_{p,z}/E_{p,z}$	E_{ratio}	$E_{p,z}$ (keV)	E_{iso} (10^{52} erg)	$L_{\text{X,11}}$ (10^{45} erg s $^{-1}$)	$E_{\text{iso}}/L_{\text{X,11}}$	$T_{p,op}$ s	Γ_{op}	$\Gamma_{op}/\Gamma_{\text{max}}$	L_{iso} (10^{52} erg s $^{-1}$)
100414A	1.39	9.2	0.020	1.640	1490.0 ± 29.0	76.900			34.7	622.0	1.040	7.000
090812	2.45	9.5	0.449	3.060	2020.0 ± 908.0	27.18	6.525	4.166	47.9	583.0	0.902	9.550
160629A	3.33	14.9	0.074	1.580	1280.0 ± 95.0	47.000			81.3	531.0	0.832	9.100
100728B	2.11	3.9	0.116	1.000	404.0 ± 47.0	2.66	0.841	3.163	33.9	462.0	1.076	1.860
050502A	3.79			1.025	498.9	3.981			57.5	461.4	0.989	2.600
080804	2.2	10.6	0.056	1.370	809.0 ± 45.0	11.500	3.181	3.615	63.1	437.0	0.928	2.690
081008	1.97			0.438	267.3	4.19	0.915	4.579	162.2	261.5	0.961	0.300
080310	2.42			0.087	75.0	3.25	1.78		182.0	255.8	0.881	0.390
									(2000)	(104)	(0.352)	
081007	0.53	6.5	0.246	0.178	61.0 ± 15.0	0.170			123.0	152.0	0.908	0.043

TABLE 8

THE OBSERVED QUANTITIES, INFERRED EFFICIENCY, AND THE PROPERTY OF EXTENDED EMISSION FOR THE SHORT GRBS.

$\epsilon_{\gamma} \lesssim 50\%$ sub-sample (8 bursts)						
GRB	z	$E_{p,z}$ (keV)	E_{iso} (10^{52} erg)	$L_{\text{X,11}}$ (10^{45} erg s $^{-1}$)	$E_{\text{iso}}/[(3.7*L_{\text{X,11}})/(1+z)/2]$	E_{ratio}
051221A	0.5465	$677.0^{+200.0}_{-141.0}$	0.91	0.277	0.687	0.296
070724A	0.457	119.5 ± 7.3	0.0016	0.0271	0.0116	0.243
070809	2.187	464.0 ± 223.0	0.104	0.338	0.133	0.368
130603B	0.356	$823.0^{+83.0}_{-71.0}$	0.196	0.0773	0.465	0.64
131004A	0.71	202.0 ± 51.0	0.068	0.145	0.109	0.14
140903A	0.351	60.0 ± 22.0	0.0044	0.285	0.00281	0.0691
150423A	0.22	146.0 ± 43.0	0.00075	0.0701	0.00176	0.408
160821B	0.16	97.4 ± 22.0	0.012	0.0115	0.164	0.0944
$\epsilon_{\gamma} \gtrsim 50\%$ sub-sample (4 bursts)						
GRB	z	$T_{90,i}$ s	$L_{\text{X,11}}$ (10^{45} erg s $^{-1}$)	$E_{\text{iso}}/[(3.7*L_{\text{X,11}})/(1+z)/2]$	E_{iso} (10^{52} erg)	$E_{p,z}$ (keV)
070714B	0.923	0.65	0.040	4.127	0.640	1060^{+285}_{-215}
110402A	0.805	2.8	0.255	1.454	1.520	1924^{+767}_{-451}
150424A	0.30	0.21	0.177	0.431	0.434	1191^{+64}_{-61}
160410A	1.717	0.58	0.441	7.749	9.300	3853^{+1399}_{-973}
170817A	0.00968	0.50		$(4.7 \pm 0.7) \times 10^{-6}$	$65.6^{+35.3}_{-14.1}$	$(1.6 \pm 0.2) \times 10^{-6}$
061006A	0.4377	0.26		0.382	909^{+260}_{-191}	0.0674
071227A	0.384	1.30			875^{+287}_{-290}	0.0196
080123A	0.495	0.27		0.32	2228^{+1272}_{-1308}	0.0398
061210A	0.4095	0.07			761^{+648}_{-64}	0.0422
060614A	0.1254	4.4		0.24	340^{+241}_{-96} ^a	0.0765
050709A	0.1606	0.06			$96.3^{+20.9}_{-13.9}$ ^a	
050724A	0.2576	2.4		0.009	138^{+503}_{-57} ^a	

^a Only detected by *Swift* or HETE-2 (lacking the detections in the high-energy band).